

# Synergistic Fusion of Aerosol Optical Depth over India from Multi-Sensor Satellite Retrievals with Ground-based Measurements

Shiba Shankar Gouda<sup>1,2</sup>, Mukunda M. Gogoi<sup>1</sup>, S Suresh Babu<sup>1</sup>

<sup>1</sup>Space Physics Laboratory, Vikram Sarabhai Space Centre, ISRO, Thiruvananthapuram, 695022, India

<sup>2</sup>Research Centre, Department of Physics, University of Kerala, Thiruvananthapuram, 695034, India

**Correspondence:** Dr. Mukunda M Gogoi ([dr\\_mukunda@vssc.gov.in](mailto:dr_mukunda@vssc.gov.in))

## Abstract

Synergistic fusion of aerosol parameters from multi-sensor measurements is crucial for integrating diverse data sources and generating consistent representations of aerosol distribution for accurate climate impact assessment. In this study, satellite observations from MODIS (Moderate Resolution Imaging Spectroradiometer) and MISR (Multi-angle Imaging SpectroRadiometer) are combined with ground-based measurements from Multi-Wavelength solar Radiometer (MWR) and CIMEL sun-photometers from the ARFINET and AERONET respectively to generate fused Aerosol Optical Depth (AOD) fields over India. The primary focus of this study is to develop a fusion framework over India, involving the evaluation and comparison of two approaches Universal Kriging (UK) and novel hybrid geostatistical-machine learning approach (RK-ML). Both methods share the same geostatistical foundation (variogram-based spatial-modelling) but differ in how the mean structure of AOD is estimated. In UK, satellite-derived AOD serves as deterministic trend for spatial prediction and is effective when ground based observations are well distributed, whereas RK-ML considers SVR-predicted AOD as prior and applies Ordinary Kriging to interpolate residuals from real-time ground observations, maintaining a near-zero residual mean away from observations which reduces distortion under sparse and uneven data conditions. Our results highlight seasonal fused AOD maps (winter, pre-monsoon, and post-monsoon) over India. Leave-One-Out Cross-Validation (LOOCV) is adopted as an evaluation strategy for assessing model performance, showing that the 95% confidence interval ( $\pm 2\sigma$ ) of the fused AOD captures over 80% of ground observations, indicating effectiveness in capturing regional aerosol variability. RK-ML demonstrates more stable spatial patterns and improved LOOCV performance compared to UK, particularly in regions with limited ground-based coverage.

**Keywords:** Aerosol Optical Depth, Universal Kriging, RK-ML, ARFINET, AERONET, MODIS, MISR

## 46 **1. Introduction**

47 Atmospheric aerosols play a significant role in introducing uncertainties into climate change  
48 projections. Although various factors such as microphysical parameters and chemical  
49 composition are important, aerosol optical depth (AOD), quantified by the total amount of  
50 columnar aerosol loading in the atmosphere, is the most critical parameter for understanding  
51 their climate forcing effects. With advances in technology and retrieval-algorithms, the  
52 number of satellites and ground-based observations of AOD is increasing. Although satellites  
53 are known to capture spatial heterogeneity of AOD, there could be bias or uncertainty (Huang  
54 et al., 2021) compared to ground-based measurements. Even if different satellites observe the  
55 same aerosol load over the same region nearly at the same time, the retrieved AOD differs  
56 due to the differences in algorithms, calibration, and resolution of the sensors (Kinne, 2009;  
57 Schutgens et al., 2020). The geographical complexity also challenges satellites to accurately  
58 retrieve AOD over highly heterogeneous land surfaces. On the other hand, data from ground-  
59 based sensors, though sparsely distributed, are more reliable than satellite measurements due  
60 to improved accuracy of measurement and retrieval procedure (Holben et al., 1998; Moorthy  
61 et al., 2007). Thus, the discrepancy between various satellite measurements and between  
62 satellite- and ground-based measurements of AOD is a serious concern in accurately  
63 characterizing aerosol loading over different parts of the globe (Wong et al., 2013; Sogacheva  
64 et al., 2020). In this context, there is a considerable effort in improving aerosol retrieval  
65 accuracy using approaches such as synergy processing of sun-photometer and lidar  
66 observations (Jin et al., 2025), synergistic retrieval from multi-mission space-borne  
67 measurements (Litvinov et al., 2025), gap-filling based on improved tensor-flow-based  
68 method (Bai et al., 2024), and the application of physics-informed deep-learning framework  
69 to multi-angle polarimetric measurements (Tao et al., 2023). Several studies have reported  
70 that if the correlations between the AOD from multiple ground-based and space-based  
71 sensors are sufficiently strong (Liu et al., 2004; Jiang et al., 2007; Prasad and Singh, 2007),  
72 then these observations can be used together for optimal characterization of aerosol features  
73 over a broader region. Thus, there is a growing demand for fused products to address  
74 limitations and achieve an optimal outcome, thereby strengthening reliability of aerosol  
75 database (Kahn et al., 2023).

76 Several approaches have previously been developed for multi-sensor data fusion involving  
77 satellite-to-satellite and satellite-to-ground observations. One notable method is the use of  
78 point spread function (PSF) modeling for single scanning footprints (Gupta et al., 2008).  
79 While PSF-based techniques are widely applied in image fusion, they face challenges in  
80 achieving accurate spatiotemporal collocation across different satellite platforms and don't  
81 show applicability regarding ground based AOD fusion rather solely on satellite footprint as a  
82 weighting factor for the merging of AOD from different sensors, such as MODIS (Moderate  
83 Resolution Imaging Spectroradiometer) and MISR (Multi-angle Imaging SpectroRadiometer)  
84 and Clouds and the Earth's Radiant Energy System (CERES). Statistical approaches such as  
85 Maximum Likelihood Estimation (Kim et al., 2024; Nirala, 2008) and Bayesian Maximum  
86 Entropy (Tang et al., 2016) have been applied to integrate satellite and ground-based  
87 observations. These methods explicitly account for uncertainty; but, their practical  
88 implementation is often limited by high computational demands, as they require large datasets  
89 for effective sampling and detailed pixel-level uncertainty characterization to produce reliable

90 fused products. Similarly, approaches such as the Ensemble Kalman Filter (Li et al., 2020)  
91 improve uncertainty quantification and have been applied at the global scale; however, their  
92 application is constrained by substantial computational cost and data requirements. These  
93 limitations pose challenges for near-real-time applications and for achieving high regional  
94 accuracy, particularly in regions with limited ground-based observational support. Simpler  
95 least-squares-based approaches, including adaptive weighted estimation (Guo et al., 2013)  
96 and semi-empirical optical algorithms (Xu et al., 2012), offer computational efficiency;  
97 however, their validation and broader applicability remain uncertain. More recently, machine  
98 learning techniques, particularly deep neural networks (DNN) (Kim et al., 2024), have  
99 demonstrated comparable performance, but their dependence on large training datasets and  
100 challenges in generalization limit their practical deployment.

101 In this study, we have adapted the Kriging technique to produce optimal fused AOD products  
102 over India. Among the various data fusion techniques, Kriging has gained significant  
103 attention for its applicability under geostatistical framework and has long been recognized as  
104 a robust and effective geostatistical technique for spatial estimation (Zimmerman et al., 1999;  
105 Shi et al., 2007; Prafull Singh & Verma, 2019; Stein & Corsten, 1991; Zhao et al., 2017).  
106 Notably, though geostatistical approaches provide a promising framework for data fusion,  
107 they are constrained by high computational demands, particularly when incorporating both  
108 spatio-temporal autocorrelation and covariance matrix inversion. Hence, reduced-rank  
109 methods such as Spatial statistical data fusion (SSDF) (Puttaswamy et al., 2014; Nguyen et  
110 al., 2012) alleviate computational burden but may introduce overfitting due to more number  
111 of parameters. Under such a scenario, Universal Kriging (UK) offers more stable AOD  
112 estimates near domain boundaries owing to its simpler and more robust formulation  
113 (Puttaswamy et al., 2014). Consequently, UK has been widely adopted for multi-sensor  
114 fusion integrating satellite and ground-based observations (Chatterjee et al., 2010; Jinnagara  
115 Puttaswamy et al., 2014; Lilla and Castrignanò, 2019), although it does not explicitly account  
116 for sensor-specific uncertainties. It has been extensively applied and validated across diverse  
117 domains within atmospheric research. It has also been utilized for spatial mapping of  
118 nutrients over oceans (Zhou et al., 2014) and as well as in mining, hydrology, electro-  
119 magnetic field mapping, and remote sensing image processing (Rossi et al., 1994). The  
120 Kriging outcomes are also found to be comparable with those from DNN (Chen et al., 2020;  
121 Kadow et al., 2020).

122 Previous research over the Indian region has estimated fused AOD from ground and satellite  
123 based observations using Cressman method, which employs inverse distance weighting  
124 (IDW), a widely used Geostatistical approach (Pathak et al., 2019). In this study, AOD  
125 measurements carried out from more than 40 ground-based observatories of the Aerosol  
126 Radiative Forcing over India Network (ARFINET; **Fig.-S1a**), which constitutes the national  
127 network of aerosol observatories across India and the largest such network in South Asia, are  
128 primarily used to integrate with the satellite-based observations from MODIS (Moderate  
129 Resolution Imaging Spectrometer) and the MISR (Multi-angle Imaging Spectro-Radiometer)  
130 to generate fused AOD using UK framework. Additionally, ground-based AOD data from the  
131 AEROSOL ROBOTIC NETWORK (AERONET; **Fig.-S1b**) are utilized to enhance the robustness of  
132 the database. While Kriging approaches have been previously applied to generate fused AOD

133 over northern India, the amount of ground data included in their studies was limited (Singh  
134 and Venkatachalam, 2014; Singh et al., 2016).

135 While satellite and ground-based AOD measurements generally exhibit a linear correlation,  
136 regional and environmental factors introduce biases, noise and nonlinear dependencies  
137 between explanatory and response variables. Although nonlinear extensions within the UK  
138 framework are possible, they require sophisticated techniques to achieve optimal  
139 performance, making the hybrid approach a compelling alternative. While the trend  
140 component in UK framework is conventionally modeled using low-order polynomials (e.g.,  
141 first or second degree), studies exploring non-linear trend modeling are still relatively rare.  
142 For instance, Snepvangers et al. (2003) incorporated a logarithmic trend to improve  
143 prediction of soil water content using net precipitation as an auxiliary variable. Freier and  
144 Lieres (2015) proposed a Taylor-based linearization technique combined with iterative  
145 parameter estimation to capture non-linear trend functions in UK. Freier et al. (2017) further  
146 extended this approach to interpolate low-density, irregular biocatalytic data. These  
147 techniques are effective when the functional form of the non-linearity is known a priori.  
148 However, in most practical scenarios, such explicit formulations are unavailable due to  
149 complex, unknown interactions between design factors and responses. In this context,  
150 machine learning (ML) models, especially kernel-based methods such as Support Vector  
151 Regression (SVR), offer an effective alternative for capturing nonlinear and implicit  
152 relationships from data without the need of predefined functional forms. Considering the  
153 usefulness of prior spatial information on AOD across the domain, a hybrid Residual Kriging  
154 with Machine Learning (RK-ML) framework is adopted in this study, where SVR is used to  
155 generate an initial prediction of AOD, which serves as a prior estimate. The preference for  
156 SVR over decision-tree-based algorithms arises from its effectiveness for problems involving  
157 a small number of features and limited datasets, enabling more reliable fused estimates even  
158 when ground-based observations are sparse. While UK involves weighted regression with  
159 spatial covariance structures (for spatial predictions), RK-ML employs ML based regression  
160 and spatial covariance structure to produce more efficient and stable spatial patterns.

161 In this study, we primarily implement the UK framework over the Indian region to generate  
162 monthly fused AOD. Additionally, we evaluate and compare both the geostatistical-machine  
163 learning fusion frameworks (UK and RK-ML) while integrating satellite and ground-based  
164 AOD observations over India. We further assess the sensitivity of the fusion to the density of  
165 ground-based observations, demonstrating how sparse networks can introduce artifacts.

## 166 **2. Data and Methodology**

### 167 **2.1 Ground-based AOD**

168 The ground-based AOD is primarily obtained from ARFINET observations, having  
169 continuous measurements across the Indian region since 1985 maintained under ISRO-GBP  
170 (Gogoi et al., 2009; Babu et al., 2013). The spectral AOD measurements in the ARFINET  
171 observatories are carried out using a Multi-Wavelength solar Radiometer (MWR) and the  
172 handheld MICROTOPS-II Sun photometer. Both these instruments have been extensively  
173 inter-compared, and their consistencies have been established (Kompalli et al., 2010). The  
174 MWR is built on the principle of filter wheel radiometry. The measurements of direct solar  
175 flux using MWR are made at ten narrow wavelength bands centered at 380, 400, 450, 500,  
176 600, 650, 750, 850, 935, and 1025 nm. The AOD is estimated following the Langley

177 Technique (Shaw, 1973; Moorthy et al., 2007; Moorthy et al., 2007) after subtracting the  
 178 contribution due to molecular scattering and absorption due to O<sub>3</sub> and water vapour from total  
 179 optical depth. For this, the MWR raw data (voltage readings corresponding to the time of  
 180 acquisition) for the entire day are split into forenoon and afternoon. If the data span during  
 181 each half of the day is more than 3 hours, the Langley plot is made separately for both  
 182 forenoon and afternoon following cloud screening criteria. In order to estimate instantaneous  
 183 AOD corresponding to each MWR measurement, the time-weighted Langley Intercept (LI)  
 184 for the entire day is calculated from the forenoon and afternoon data as

$$185 \quad LI_{\text{daily}} = (LI_{\text{FN}} * T_{\text{FN}} + LI_{\text{AN}} * T_{\text{AN}}) / (T_{\text{FN}} + T_{\text{AN}}) \quad (1)$$

186 Where, T<sub>FN</sub> and T<sub>AN</sub> are the durations of MWR measurements in the forenoon and afternoon.  
 187 Based on this, the instantaneous AOD (after correcting the contributions due to Rayleigh  
 188 scattering, Ozone, and water vapor) is estimated as:

$$189 \quad AOD_{\text{ins}} = \{(LI_{\text{daily}} - \ln V) / m\} - (\tau_{\text{R}} + \tau_{\text{O}_3} + \tau_{\text{WV}}) \quad (2)$$

190 The accuracy of AOD estimates from MWR is based on the accuracy of the estimate of LI.  
 191 Since, LI is also a parameter of indirect calibration of the instrument, the temporal variability  
 192 of LI is examined to ensure performance of the system and qualify usable data. Typically LI  
 193 varies within 5% of the mean and up to 10% in worst cases. Fluctuations are more  
 194 pronounced at shorter wavelengths than at longer ones. Owing to these variations, total AOD  
 195 uncertainty ranges from 0.02 to 0.03, increasing at shorter wavelengths (<500 nm) and during  
 196 high AOD conditions (>0.5), which are mainly limited to the pre-monsoon season.  
 197 Importantly, these errors are primarily statistical and uncorrelated across channels, rather than  
 198 systematic (e.g., dark current, detector offsets, and molecular scattering/absorption modelling  
 199 which are <0.1%). The instrument details, AOD retrieval method, and error budget have been  
 200 discussed elsewhere Gogoi et al., 2009; Babu et al., 2013; Kompalli et al., 2010; Moorthy et  
 201 al., 2007).

202 Apart from MWR, AOD is obtained from handheld MICROTOPS-II sun-photometer (Solar  
 203 Light Company, USA) at five wavelengths (440, 500, 675, 870, and 936 nm). MICROTOPS-  
 204 II can achieve AOD estimates with accuracy comparable to CIMEL Sun photometers used in  
 205 the AERONET network, with uncertainties ranging from 0.01 to 0.02, as reported by Ichoku  
 206 et al. (2002). In addition to ARFINET measurements, simultaneous AOD products (version 3,  
 207 level 2.0) available within the study region from AERONET measurements are used. The  
 208 CIMEL sun-photometers in AERONET measure AOD at 340, 380, 440, 500, 675, 870, and  
 209 1020 nm in a time interval of 5 to 15 min for cloud-free conditions with an uncertainty ~ 0.01  
 210 - 0.02 (Eck et al., 1999; Holben et al., 1998; Giles et al., 2019). To use the ARFINET and  
 211 AERONET AOD in the fusion experiment, the AOD values are interpolated to 550 nm  
 212 (corresponding to MODIS and MISR AOD) using the methodology of Liu et al. (2004):

$$213 \quad \ln \left( \tau_{\lambda_1} / \tau_{\lambda_2} \right) = -\alpha \ln \left( \lambda_1 / \lambda_2 \right) \quad (3)$$

214 Where,  $\tau_{\lambda_1}$  and  $\tau_{\lambda_2}$  are AODs at wavelengths  $\lambda_1$  and  $\lambda_2$ , respectively and  $\alpha$  is Angstrom  
 215 Exponent.  $\alpha$  is determined by applying linear least squares fit to the logarithmic values of  
 216 AOD measured at various wavelengths. For this study, values of  $\alpha$  were estimated from the

217 wavelength dependent relationship of AOD at 450 and 650 nm for MWR, and 440 and 670  
218 nm pair for CIMEL. Using this, AOD at 550 nm was estimated; where the base AOD was  
219 taken at 500 nm (in case missing AOD at 500 nm, base AOD at 440 or, 450 nm was  
220 considered).

## 221 **2.2 Satellite retrieved AOD**

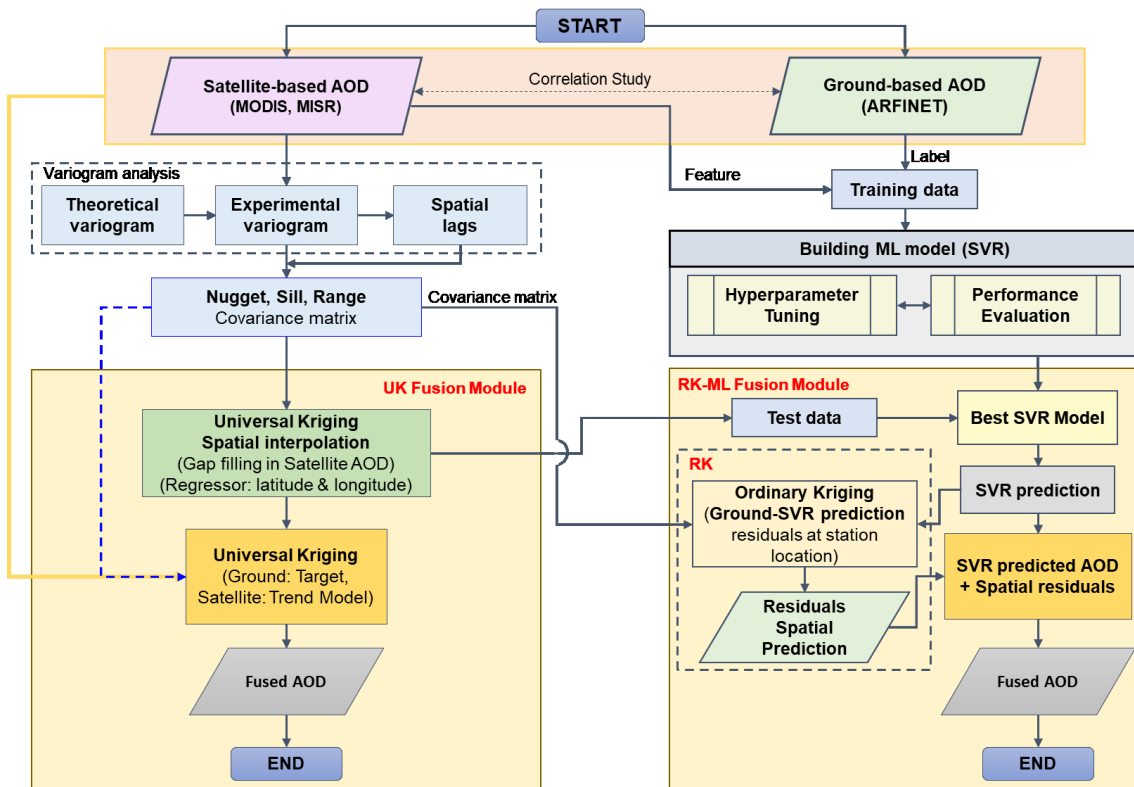
222 The satellite-based AOD for this study is obtained from MODIS and MISR. MODIS data  
223 (Collection 6.1 Level-2 AOD at 550 nm; 'AOD\_550\_Dark\_Target\_Deep\_Blue\_Combined';  
224 spatial resolution of 10 km; over land) is obtained from NASA's Level-1 and Atmosphere  
225 Archive and Distribution System Distributed Active Archive Center (LAADS DAAC). The  
226 merged AOD product combines only high-quality Dark Target (DT; QA = 3 over land, QA >  
227 0 over ocean) and Deep Blue (DB; QA = 2 and 3) retrievals to provide global 10 km  
228 coverage. Over land, selection is based on Normalized Difference Vegetation Index (NDVI),  
229 with DB used for bright (arid, semi-arid) surfaces ( $NDVI \leq 0.2$ ), DT for vegetated (darker)  
230 regions ( $NDVI \geq 0.3$ ). In transitional zones, the higher-QA retrieval or their average is  
231 applied, while over ocean only DT is used. Although this approach improves spatial coverage  
232 and usability, uncertainties may arise in averaged regions and due to assumptions about  
233 algorithm performance across surface types (Sayer et al., 2014). Sensitivity studies across  
234 diverse land surfaces employing various algorithms have validated that integrating the DT  
235 and DB methods yields enhanced accuracies, but errors persistently emerge over South Asia  
236 (Gao et al., 2021; Tian et al., 2018; Wei et al., 2019). Furthermore, the performance of the  
237 product has been evaluated across different seasons (Sharma et al., 2021). Overall, an  
238 expected error of  $0.05 \pm 0.15 \times AOD$  for DT and  $0.05 \pm 0.20 \times AOD$  for DB over the land  
239 and  $0.03 \pm 0.05 \times AOD$  over the ocean is reported in most studies (Levy et al., 2005; Sayer et  
240 al., 2013; Tian et al., 2018; Tian and Gao, 2019; Wei et al., 2019).

241 The MISR AOD (version V23) is obtained from Atmospheric Science Data Centre (ASDC).  
242 MISR V23 products provide aerosol information with a spatial resolution of  $4.4 \text{ km} \times 4.4 \text{ km}$   
243 (Garay et al., 2017; Sayer et al., 2020; Witek et al., 2018, 2021). Theoretical sensitivity  
244 studies and performances for MISR (Kahn et al., 2001; Tao et al., 2020) have projected  
245 standard deviations of the measurement error associated with optical depth to be  $\pm (0.05 +$   
246  $20\%AOD_{AERONET})$ , showing a consistently narrower range over ocean compared to bright  
247 land surfaces.

248 The MODIS and MISR datasets used in this study are both acquired from the Terra satellite  
249 platform and therefore have nearly identical overpass times. This temporal consistency  
250 ensures improved compatibility in the fusion process and minimizes uncertainties associated  
251 with diurnal variability in aerosol loading. In contrast, inclusion of MODIS observations from  
252 the Aqua satellite, which has a different overpass time, would introduce additional variability  
253 related to diurnal aerosol evolution that requires explicit treatment. Addressing such effects is  
254 beyond the scope of the present methodology-focused study and will be considered in future  
255 work. In the fusion approach, MODIS AOD represents high-quality retrievals (QA = 2, 3),  
256 while MISR exhibits minimal retrieval uncertainties (0.02–0.08) over ground stations.  
257 Additional screening or filtering was not applied beyond these criteria, as it may attenuate the  
258 inherent systematic bias between ground- and satellite-based observations. Quality-assured  
259 and expected-error-based filtering can be considered as part of the future scope of the study to  
260 enable more accurate inferences.

261 **2.3 Fusion methodology**

262 The geostatistical data fusion method used in this study combines spatial data from multiple  
 263 sources (satellite and ground-based, as detailed in Sections 2.1 and 2.2) with varying  
 264 resolutions, accuracies, and types of measurements. The aim is to enhance the overall  
 265 understanding and prediction of spatial variables (e.g., AOD) to produce a more accurate and  
 266 comprehensive representation of columnar AOD, with an emphasis on reducing inter-sensor  
 267 biases through integration with ground-based observations. For this, we have adapted UK  
 268 framework, where data interpolation relies on unknown functions (e.g., satellite derived  
 269 AOD) represented as trend models with spatial autocorrelation through variogram analysis.  
 270 Building on this framework, the fusion methodology is designed to operate under practical  
 271 observational constraints, such as differences in sensor characteristics (e.g., spatial coverage,  
 272 revisit frequency, and collocation with ground observations), which limit consistent data  
 273 availability at daily timescales. Hence, the analysis is conducted at the monthly scale to  
 274 improve spatial representativeness, reduce sampling gaps, and enhance statistical robustness.  
 275 Notably, the monthly satellite AOD products also retain sensor-specific biases and inter-  
 276 product inconsistencies. Thus, the fusion approach presented here is not primarily aimed at  
 277 gap-filling, but at generating a more accurate and internally consistent AOD dataset by  
 278 integrating complementary information from multiple sensors and ground-based observations.  
 279 Thus, even at the monthly scale, the proposed method adds value by reducing retrieval  
 280 uncertainties and improving the reliability of aerosol distributions, which is critical for  
 281 climate studies and radiative forcing assessments. The overview of the fusion method is  
 282 presented in **Fig. 1**, followed by a detailed description of each step in the following sections.



283  
 284 **Figure 1.** Flowchart of fusion methodology: Universal Kriging (UK) and Residual Kriging  
 285 Machine Learning (RK-ML). The machine learning best model is designed based on the long  
 286 term MODIS and MISR data which were collocated with ground-based observations.

### 287 **2.3.1 Correlation analysis**

288 As a first step of the fusion processes, the correlation analysis between the satellite and  
289 ground-based AOD was made to understand the association/ biases between the two data sets  
290 at different spatiotemporal scales. This is useful to understand the requirement of multi-sensor  
291 data fusion. For this, a statistical spatio-temporal matching approach (similar to those  
292 reported elsewhere by Basart et al., 2009; Chu et al., 2002; Filonchyk et al., 2019; Ichoku et  
293 al., 2002) was applied, in which satellite observations were spatially averaged at  $0.5^\circ$  spatial  
294 resolution and compared with ground-based AOD averaged within a 30 minute time window  
295 around the overpass time of the TERRA satellite which accommodated 14 to 15  
296 measurements from MWR (data frequency 2 min) and 1 to 2 measurements from CIMEL  
297 (data frequency 15 min) observations. Although satellite products such as MODIS ( $\sim 10$  km)  
298 and MISR ( $\sim 4.4$  km) provide higher spatial resolution potentially capturing finer regional  
299 variability in aerosol distributions, yet their direct comparison with ground-based point  
300 measurements introduces representativeness errors due to scale mismatch. Aggregating the  
301 data to a coarser grid ( $0.5^\circ$ ) reduces this mismatch by ensuring that both satellite and ground  
302 observations represent comparable spatial scales, thereby improving the robustness of  
303 validation and fusion. Thus, the choice of  $0.5^\circ$  represents an optimal choice, yielding higher  
304 correlation and lower root mean square error (RMSE) (**Figs. S2a, b**), in addition to retaining  
305 regional variability and ensuring sufficient data density within each grid cell for stable  
306 statistical estimation and fusion. The consideration of  $0.5^\circ$  resolution is in line with approach  
307 adopted by Tandule et al. (2026) for retrieving AOD from satellite observations, ensuring  
308 improved representativeness and temporal consistency in comparisons between satellite-  
309 derived and ground-based AOD. In addition, generating AOD at this resolution provides a  
310 valuable reference dataset for comparison and validation against reanalysis products and  
311 model outputs of AOD, where satellite observations are commonly assimilated as primary  
312 inputs. Further, AOD observations in this study were aggregated to a monthly scale to ensure  
313 more consistent spatial coverage and improve the reliability of multi-sensor fusion analysis.  
314 Due to the differences in spatial coverage and revisit characteristics of MODIS and MISR as  
315 well as temporal gaps in data availability from ground-based instruments (**Figs. S3a, 3b, 3c**),  
316 daily datasets often contained substantial spatial gaps over the study domain.

### 317 **2.3.2 Variogram Analysis**

318 Variogram analysis is used to quantify and model the spatial autocorrelation (i.e., spatial  
319 dependence) of a dataset. It evaluates how the spatial variability between data points changes  
320 as a function of lag distance, the distance separating two sample points in space. To capture  
321 the spatial dependency of the data, geographical parameters such as latitude, longitude, and  
322 elevation are often incorporated as covariates in the trend function, thereby incorporating the  
323 spatial context of the sampling locations. This approach has been widely applied in studies  
324 involving meteorological parameters (Chua and Bras, 1982; Holdaway, 1996; Nalder and  
325 Wein, 1998). In the present context, spatial representation of AOD is fairly represented as a  
326 trend function comprising of latitude, longitude, and elevation, which serve as proxies for  
327 underlying spatial variations of geographical and atmospheric influences that significantly  
328 affect aerosol distribution. However, it is important to note that most geostatistical methods,  
329 such as Kriging, assume the underlying field to follow second order or, intrinsic stationarity  
330 (mean is constant, and the covariance or, variance of increments depends only on spatial lag).

331 However, real-world environmental and geophysical data often exhibit large-scale spatial  
332 trends driven by physical and geographical factors, such as latitude, longitude, and elevation.  
333 In the case of AOD, these variables act as key spatial predictors that capture dominant  
334 regional gradients and can be used to model and remove the large-scale spatial trend. In the  
335 presence of strong spatial trends, variogram may become unbounded or exhibit unrealistically  
336 large ranges. These spatial trends violate the stationarity assumption which can lead to  
337 unbounded variogram. To address this spatial detrending of the data is performed, which  
338 isolates the local fluctuations or residuals from the spatial data set. This serves as an essential  
339 step in geostatistical analysis to ensure a well-defined and bounded variogram, enabling  
340 reliable estimation of sill, nugget, and range parameters for spatial covariance modeling. To  
341 validate this assumption, we obtained the frequency distribution of satellite AOD and their  
342 residuals (**Fig. S4**) after detrending. A nearly symmetric histogram of detrended residuals  
343 indicates that the trend component has been effectively removed, which is a prerequisite for  
344 second-order stationarity (Tang et al., 2016). Since the detrending in our study is purely a  
345 spatial operation, the temporal dimension is not explicitly considered and is effectively  
346 treated as constant during the detrending process. Consequently, the approach does not  
347 involve long-term datasets or explicitly account for seasonal variability (e.g., all four  
348 seasons).

349 The semivariance, which measures the degree of spatial variability between pairs of sample  
350 points as a function of their separation distance, known as the lag-distance ( $h$ ), is calculated  
351 as:

$$352 \quad \gamma(h_x) = 1/2n(h) (\sum [z(x_i) - z(x_i + h)]^2) \quad (4)$$

353 Where  $z(x_i)$  and  $z(x_i+h)$  are the values of the variables of interest at locations  $x_i$  and  $x_i + h$  (=  $x_j$ ), respectively;  $n(h)$  is the number of pairs of points separated by the lag-distance  $h$ , which  
355 is given as:

$$356 \quad h_x = r \cos^{-1}(\sin \varphi_i \sin \varphi_j - \cos \varphi_i \cos \varphi_j \cos(\theta_i - \theta_j)) \quad (5)$$

357 Where  $\varphi_{i,j}$  represent longitudes of locations  $x_i$  and  $x_j$ , and  $\theta_{i,j}$  represent latitudes of locations  
358  $x_i$  and  $x_j$ ;  $r$  is the mean radius of the earth. Following this, the empirical variogram is  
359 calculated from the actual observational data, showing the relationship between semivariance  
360 and lag distance for each set of observations. The experimental variogram is obtained after  
361 binning semivariance at certain lags of the empirical variogram. The experimental variogram  
362 is then fitted with a theoretical model to describe the spatial continuity of the variable. The  
363 theoretical models considered in the present study include Exponential, Spherical, and  
364 Matheron models; the mathematical expressions are given as:

$$365 \quad \gamma_{theo}(h_x) = \begin{cases} 0 & h_x = 0 ; \\ \sigma_n^2 + \sigma_b^2 (1 - \exp(-h_x/l)) & h_x > 0 \end{cases} \quad \text{(Exponential)} \quad (6)$$

$$366 \quad \gamma_{theo}(h_x) = \begin{cases} 0 & h_x = 0 ; \\ \sigma_n^2 + \sigma_b^2 \left( 3h_x/2l - 1h_x^3/2l^3 \right) & 0 < h_x \leq l ; \\ \sigma_n^2 + \sigma_b^2 & h_x > l \end{cases} \quad \text{(Spherical)} \quad (7)$$

$$367 \quad \gamma_{theo}(h_x) = \begin{cases} 0 & h_x = 0; \\ \sigma_n^2 + \sigma_b^2 \left( 1 - \exp\left(-h_x^2/l^2\right) \right) & h_x > 0; \end{cases} \quad \text{(Matheron)} \quad (8)$$

368 In the above equations,  $\sigma^2 = \sigma_n^2 + \sigma_b^2$ , represents the total variance observed in AOD data at  
369 larger lag distances (spatially uncorrelated AOD data).  $\sigma_n^2$  is nugget (y-intercept of the  
370 variogram), which represents the semivariance at a very small lag distance, approaching zero.  
371 Nugget (spatial variation at distances smaller than the smallest sampling interval) is indicative  
372 of the presence of measurement error or noise in the data. A large nugget relative to the sill  
373 (i.e., the semivariance value where the variogram levels off, representing maximum  
374 variability or correlation between data points at a given spatial distance) suggests significant  
375 measurement error or unresolved variability. This can indicate potential issues with data  
376 quality. On the other hand, a small nugget implies that the data is relatively free of noise and  
377 that most of the spatial variability is due to the structured spatial process.  $\sigma_b^2$  is variance in  
378 spatially correlated data, and this parameter gradually increases with increasing lag distances  
379 until it reaches sill.  $l$  is the range parameter, the distance at which the semivariance reaches  
380 the sill; up to this distance, data are spatially correlated with each other. The higher the range,  
381 the more similar the values are at greater distances from each other. The spatial covariance  
382 function can be derived from the variogram model as:

$$383 \quad C_{ij} = \sigma^2 - \gamma_{theo} \quad (9)$$

### 384 2.3.3 Universal Kriging

385 Universal Kriging (UK) also referred to as Kriging with a trend model, extends Ordinary  
386 Kriging by incorporating a deterministic trend component alongside the stochastic spatial  
387 component. This approach is useful when there is an underlying trend in the data that varies  
388 across the study area. The UK method uses both the spatial autocorrelation structure and the  
389 deterministic trend to make predictions. The UK model can be expressed as:

$$390 \quad Z = M_z\beta + \epsilon \quad \text{Or, } \epsilon = Z - M_z\beta \quad (10)$$

391 Where,  $Z = [Z(x_1), Z(x_2), \dots, Z(x_n)]^T$  represent the values of the variables of interest at  
392 locations  $x_1, x_2, \dots, x_n$ , respectively.  $M_z$  is the deterministic trend component of the model  
393 ( $n \times p$ ) where  $p$  is representing the number of regressors; and  $\beta$  is the unknown drift  
394 coefficient ( $p \times 1$ ) to be estimated;  $\epsilon$  is the stochastic component or stochastic residuals  
395 ( $n \times 1$ ), i.e., mean zero random fields.

396 In the present study, the trend component  $M_z$  for fusion is defined as

$$397 \quad M_z = \begin{pmatrix} 1 & MODIS_{AOD_1} & MISR_{AOD_1} \\ 1 & MODIS_{AOD_2} & MISR_{AOD_2} \\ \vdots & \vdots & \vdots \\ 1 & MODIS_{AOD_n} & MISR_{AOD_n} \end{pmatrix} \quad (11)$$

398 This is similar to a multiple regression model, which is described through a combination of a  
399 constant term and two sensor measurements that act as regressors to predict AOD at  
400 estimation locations. The first component of this trend model represents the overall offset  
401 (i.e., the mean of the portion of the AOD distribution that is not captured by MISR and

402 MODIS). This constant term thereby represents any systematic offset between the combined  
 403 (MISR and MODIS) satellite-retrieved AOD and the ground-measured AOD.

404 Following equation (10), the expected value at prediction locations ( $x_s$ ) can be expressed as  
 405 the best linear unbiased prediction (BLUP):

$$406 \hat{Z}(x_s) = m_s^T \hat{\beta} + C_{zs}^T C_{zz}^{-1} (Z - M_z \hat{\beta}) \quad (12)$$

407 Here,  $C_{zs}(n \times s)$  is the spatial covariance matrix of the residuals between the sample location  
 408 (i.e., measurement locations) and prediction locations (i.e., estimation locations) and  $C_{zz}(n \times$   
 409  $n)$  is the spatial covariance matrix of the residuals between the sample locations (i.e.,  
 410 measurement locations) as obtained from equation (9). The unknown coefficient  $\hat{\beta}$  can be  
 411 expressed as the generalized least squares (GLS) estimator from the covariance matrix,

$$412 \hat{\beta} = (M_z^T C_{zz}^{-1} M_z)^{-1} M_z^T C_{zz}^{-1} Z \quad (13)$$

413 Alternatively, minimizing the mean square error (MSE) of all predictions among the  
 414 predictors of the form  $\lambda^T Z$  subjected to unbiasedness constraint, i.e.,  $E(\lambda^T Z) = E(Z(x_s))$  for  
 415 all  $\beta$ , which is identical to  $\lambda^T M_z \hat{\beta} = m_s^T \hat{\beta}$  and under conditions for minimizing variance  
 416 ( $\lambda^T Z - Z$ ), Lagrange multipliers ( $\mu(p \times s)$ ) are used to solve the linear constraint equations  
 417 as given below,

$$418 \begin{bmatrix} C_{zz} & M_z \\ M_z^T & 0 \end{bmatrix} \begin{bmatrix} \lambda \\ \mu \end{bmatrix} = \begin{bmatrix} C_{zs} \\ m_s \end{bmatrix} \quad (14)$$

419 Here,  $M_z(n \times p)$  and  $M_z^T(p \times n)$  are trend models of AOD given by equation (11);  $m_s$   
 420 ( $p \times s$ ) is trend model at  $s$  estimation locations;  $\lambda(n \times s)$  are the Kriging weights,  $\mu$  is the  
 421 Lagrange multiplier.

422 The system of equations is solved for Lagrange multiplier  $\mu$  and weights  $\lambda$  to estimate AOD  
 423 at estimation locations. This can be expressed as:

$$424 \begin{bmatrix} \lambda \\ \mu \end{bmatrix} = \begin{bmatrix} C_{zz} & M_z \\ M_z^T & 0 \end{bmatrix}^{-1} \begin{bmatrix} C_{zs} \\ m_s \end{bmatrix} \quad (15)$$

$$425 \lambda = \{C_{zz}^{-1} - C_{zz}^{-1} M_z (M_z^T C_{zz}^{-1} M_z)^{-1} M_z^T C_{zz}^{-1}\} C_{zs} + C_{zz}^{-1} M_z (M_z^T C_{zz}^{-1} M_z)^{-1} m_s \quad (16)$$

$$426 \lambda^T Z = C_{zs}^T C_{zz}^{-1} (Z - M_z \beta) + m_s^T \beta \quad (17)$$

427 The prediction variance associated with predicted values can be represented as

$$428 \text{Var}(Z(x_s) - \hat{Z}(x_s)) = \sigma_{Z(x_s)}^2 - C_{zs}^T C_{zz}^{-1} C_{zs} + (m_s^T - (M_z^T C_{zz}^{-1} C_{zs})^T)^T (M_z^T C_{zz}^{-1} M_z)^{-1} (m_s^T - (M_z^T C_{zz}^{-1} C_{zs})^T) \quad (18)$$

429 The above weighting approach determines the values at prediction locations. **Our foremost**  
 430 **approach involved creating a trend model for fusion. For this purpose, we generated a**  
 431 **complete satellite-based map of AOD from MODIS and MISR separately over the study**  
 432 **region using the UK method. In this framework, geographical parameters such as latitude,**  
 433 **longitude and elevation are treated as regressors (trend model), whereas observed satellite**  
 434 **data serve as response variables to fill the gaps in individual satellite datasets.** Subsequently,  
 435 in the final spatial fused predictions, the ground-based AODs were treated as the response  
 436 variables, where the satellite data, along with the elevation model (used as additional  
 437 information), were used as regressors.

438

### 439 2.3.4 Residual Kriging Machine Learning (RK-ML)

440 The RK-ML approach is implemented in this study through a hybrid approach to generate  
 441 reliable estimates of fused AOD, with improved predictive accuracy using a limited of  
 442 ground-based observations. Although UK and the proposed RK-ML approach appear  
 443 methodologically different, they share a common conceptual foundation. From a generalized  
 444 regression perspective, both methods rely on a covariance structure to characterize spatial  
 445 dependence among grid points. However, when the number of observations is limited, the  
 446 statistical parameters in UK can adversely affect predictions at estimation locations. To  
 447 overcome the limitations associated with limited observations, SVR is employed due to  
 448 robustness of its regularized formulation in both regression and classification tasks (Sifaou et  
 449 al., 2021), where predictions are learned from datasets within a historical training window.  
 450 These predictions provide prior information on ground-based AOD that is independent of the  
 451 spatial configuration of the current ground based-observations.

452 The best-performing SVR model is first identified based on a time window of five years of  
 453 data (simultaneous MODIS, MISR and ground measurements) for a specific month (season)  
 454 targeting consistent aerosol conditions. Subsequently, this model leverages spatially  
 455 interpolated features from MODIS and MISR data (gap filled AOD by UK) to generate SVR-  
 456 predicted maps to obtain a full generalized AOD map for that month. The discrepancies  
 457 between SVR-predicted values and observed ground measurements are treated as residuals,  
 458 which are then spatially modeled using Ordinary Kriging. The resulting residual predictions  
 459 are combined with SVR outputs to produce RK-ML-based fused products. This approach  
 460 provides a robust alternative to traditional UK-based data fusion techniques by capturing  
 461 complex relationships between predictors and target variables. The detailed RK-ML  
 462 methodology is given below.

463 SVR transforms features into a higher-dimensional space, making them linearly separable and  
 464 helps improving the prediction of target variables like ground based AOD. The use of SVR in  
 465 Kriging has been reported in previous studies to improve model predictions (Wang et al.,  
 466 2008; Baisad et al., 2023). The SVR model is represented by:

$$467 \quad Z_{svr} = w^T \varphi + b \quad (19)$$

468 where  $\varphi$  is the kernel transformed input features,  $w$  is the nonzero vector normal to  
 469 hyperplane (the plane or decision boundary that best fits the  $n$  dimension input vectors while  
 470 maintaining a margin of tolerance ( $\varepsilon$ -insensitive zone) around it) and  $b \in \mathbb{R}$ . This expression  
 471 assumes that  $Z_{svr}$  exist when it approximates all  $w^T \varphi$  with  $\varepsilon$  precision for linearly separable  
 472 data. Along with it, the concept of soft margin loss function is considered which introduces  
 473 slack variable  $\xi$  (+ve) and  $\xi^*$  (-ve) to allow some points lying inside the hyperplane.

474 Hence the optimization problem is subject to minimization of

$$475 \quad \frac{1}{2} \|w\|^2 + C \sum_{i=1}^l (\xi + \xi^*) \quad \text{Such that} \begin{cases} Z - w^T \varphi - b \leq \varepsilon + \xi \\ w^T \varphi + b - Z \geq \varepsilon + \xi^* \\ \xi_i \xi_i^* \geq 0 \end{cases} \quad (20)$$

476 The regularization constant  $C$  trades off between the model complexity and empirical error up  
 477 to which deviations larger than  $\varepsilon$  can be tolerated.  $\xi$ ,  $\xi^*$  are regression errors. The detailed  
 478 explanation of SVR model is available in the literature (Smola & Schölkopf, 2004; Brereton

479 & Lloyd, 2010). In the present study, best model of SVR is decided from the minimum  
 480 RMSE between predicted AOD and real AOD after tuning its hyperparameters.

481 The residuals, which are the difference between collocated AOD of SVR predictions from  
 482 ground based AOD, are estimated from the difference between  $\hat{Z}_{svr}(x_s)$  and  $Z$ , *i.e.*,  
 483  $\hat{Z}_{svr}(x_s) - Z$ . These residuals under ordinary Kriging are modeled as  $\delta(s) = \mu +$   
 484  $\varepsilon(s)$  where  $\mu$  refers to the mean values of residuals over study domain, which resembles  
 485 similar mathematics of universal Kriging, except  $M_z$  &  $m_s = 1$  (eq. (10) to eq. (17)).  
 486 Following this, the estimated residuals at unknown locations are determined as

$$487 \quad \delta(x_s) = \lambda^T \delta(x_z)$$

488 The weighting parameter  $\lambda$  is obtained from the covariance matrices as follows

$$489 \quad \begin{bmatrix} \lambda \\ \mu \end{bmatrix} = \begin{bmatrix} C_{zz} & 1 \\ 1 & 0 \end{bmatrix}^{-1} \begin{bmatrix} C_{zs} \\ 1 \end{bmatrix} \quad (21)$$

490 The ordinary Kriging estimation contains the spatial relation while the SVR prediction  
 491 contains the optimal estimations from features (Satellite) and labels (Ground AOD). The final  
 492 fused map can then be estimated as

$$493 \quad Z = \delta(x_s) + Z_{svr}(x_s) \quad (22)$$

494 The hyperparameters of the SVR model were optimized using a grid-search strategy as part of  
 495 the training process. In this approach, predefined values for key hyperparameters - such as the  
 496 regularization parameter (C), kernel type, gamma (Y) and epsilon ( $\varepsilon$ ) - were combined to  
 497 form all possible parameter configurations, and each configuration was evaluated. For every  
 498 hyperparameter combination, model performance was assessed using the negative mean  
 499 squared error (neg-MSE) as the evaluation metric. This metric quantifies prediction error, and  
 500 allows selection of the best model by maximizing the score. Due to the limited size of the  
 501 dataset, leave-one-out cross-validation (LOOCV) was used during training instead of k-fold  
 502 cross-validation. Even though other cross-validation approaches, such as site-based, temporal,  
 503 or sample-based validation, can also be used to assess model robustness, the LOOCV was  
 504 considered the most suitable approach in this study considering the limited number of  
 505 samples and the uneven spatial distribution of ground observations. In LOOCV, the model is  
 506 trained repeatedly on all samples except one, which is used for validation. This procedure is  
 507 repeated so that each data point serves once as the validation sample. This approach  
 508 maximized the use of available data while providing an unbiased estimate of model  
 509 performance. Based on this procedure, a linear kernel was identified as the optimal choice for  
 510 the RK-ML models, which were subsequently evaluated on independent test sets (20% for  
 511 MODIS, N=318; 10% for MISR, N=71). For MODIS AOD features, the best model  
 512 configuration was C = 1, gamma = 'scale', kernel = 'linear'; for MISR AOD features, the  
 513 optimal configuration was C = 100, gamma = 'scale', kernel = 'linear'. The use of a linear  
 514 kernel suggests a predominantly linear relationship between satellite observations and  
 515 ground-based AOD. Inclusion of the regularization parameters C and gamma controls  
 516 overfitting and penalizes noisy inputs, enabling the ML framework to generate more reliable  
 517 estimates. These estimates were further corrected using spatial residuals from RK, allowing  
 518 RK-ML to outperform UK under conditions of limited or biased AOD observations. The final  
 519 models were evaluated using correlation coefficient (R), R<sup>2</sup>, mean absolute error (MAE), and

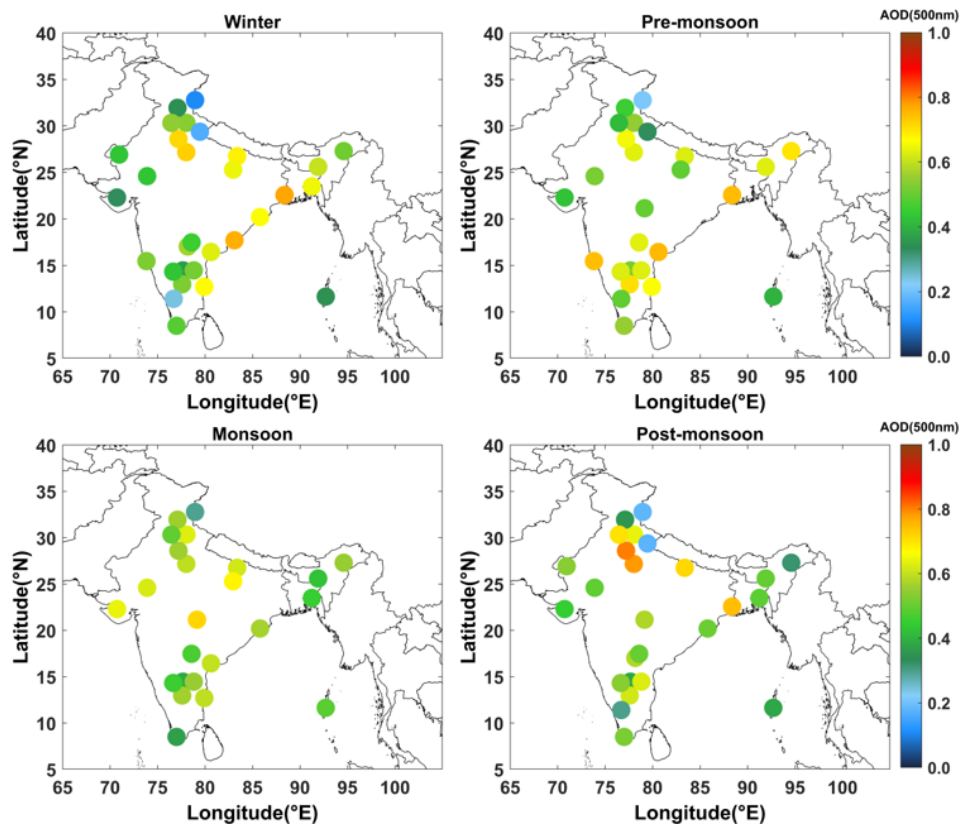
520 RMSE on both training and test sets (**Table ST1**). Results indicate that training and test  
521 performances were comparable (with training  $R^2$  values either lower or close to test  $R^2$ ),  
522 correlation coefficients were consistently high, and errors (RMSE, MAE) were low. These  
523 outcomes confirm that the SVR models did not suffer from overfitting and generalized well to  
524 unseen data, despite the limited sample size.

525 Although other machine learning algorithms, such as Random Forest (RF) and XGBoost, can  
526 also be integrated within the RK-ML framework, a sensitivity analysis conducted on MODIS  
527 test dataset indicated that SVR achieved comparable or better performance metrics ( $R$ ,  
528 RMSE; Supplementary Fig. S5).

### 529 3. Results and discussions

#### 530 3.1 Regional distribution of AOD from ground-based and satellite observations

531 The analysis of spatial distribution of AOD is crucial for understanding the consistency of  
532 measurements across different sensors. The large-scale spatial variations in the data help  
533 identify overall spatial trends over latitude-longitude and geographic elevation. Emphasizing  
534 spatial trends is also critical for assessing the mathematical assumptions underlying Kriging  
535 and variogram analysis, which rely on the condition of second-order stationarity within the  
536 sampled data. In view of this, ground-based AOD at 500 nm was considered for long-term  
537 comparison of MODIS and MISR AOD at 550 nm as the closest approximation. The typical  
538 AOD patterns over different regions over India from ground-based measurements, derived  
539 from 10 years of measurements from the ARFINET database using MWR and Microtops  
540 instruments, is illustrated in **Fig. 2**.



541

542 **Figure 2.** Long-term (2011-2020) ground-based AOD at 500 nm from MWR and  
543 MICROTOPS-II measurements in the ARFINET over the Indian region. The seasons are

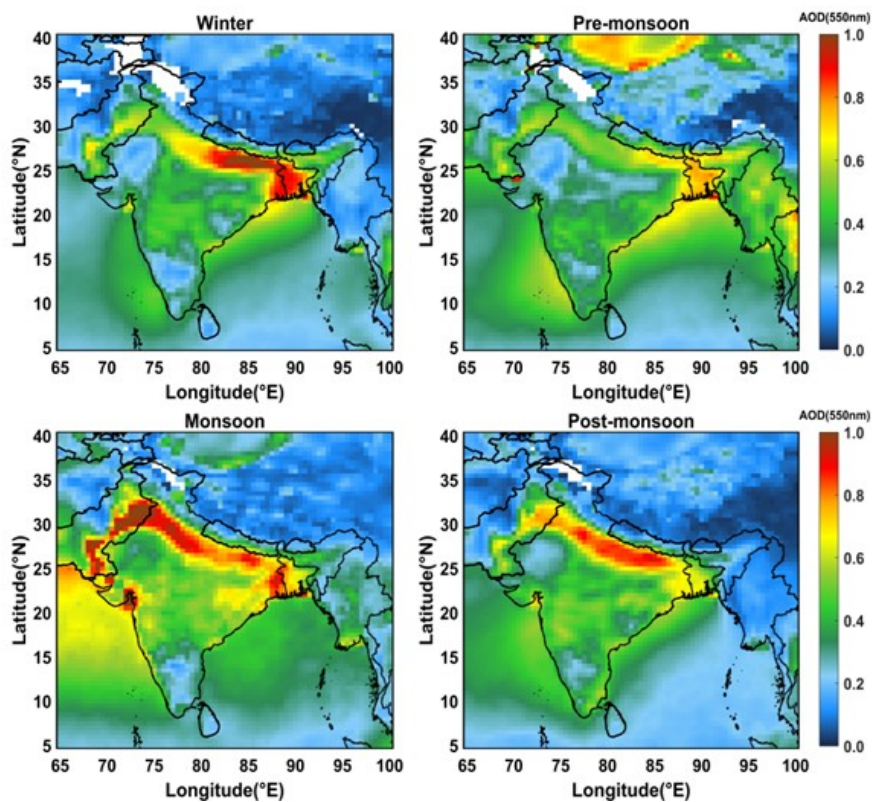
544 winter: December, January, February (DJF); Pre-monsoon: March, April, May (MAM);  
545 Monsoon: June, July, August, September (JJAS); Post-monsoon: October, November (ON).  
546 The different regions considered for representing Indo-Gangetic plane (IGP), North-west  
547 (NW), North-east (NE), Peninsular India (PI), and Central India (CI) is provided (**Fig. S6**).

548 Various factors such as the dominance of natural and anthropogenic sources, local and  
549 synoptic meteorology cause observed spatio-temporal variations in AOD at a particular  
550 location. Over most of the locations in the Indo-Gangetic Plains (IGP), AOD shows  
551 consistent high values ( $> 0.6$ ) throughout different seasons. This is similar to the observations  
552 reported by Lodhi et al., (2013); Singh et al., (2020); Tiwari et al., (2018). Next to the IGP,  
553 the north-eastern (NE) India experiences higher AOD with peak during the pre-monsoon  
554 season. Similar pattern is reported elsewhere (Gogoi et al., 2009). In Peninsular India (PI),  
555 AOD is highest during the pre-monsoon period, followed by a significant reduction during  
556 the summer monsoon. This is similar to the earlier studies by Kalluri et al., (2016); Kumar et  
557 al., (2009); Sinha et al., (2013); Vachaspati et al., (2018).

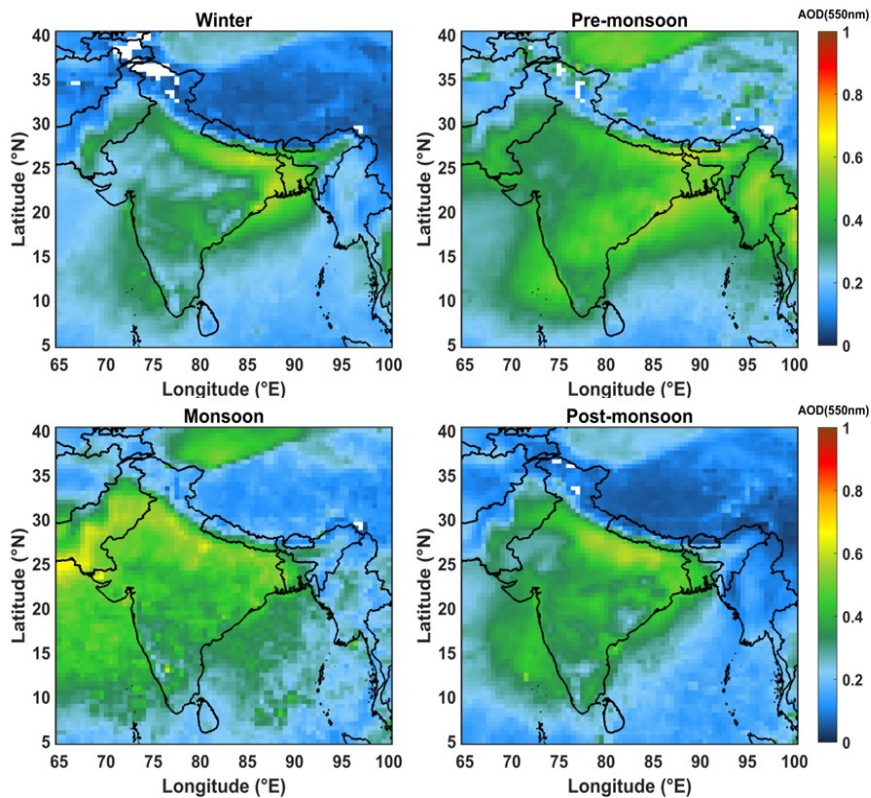
558 The spatial patterns of a decadal average satellite-based MODIS and MISR AOD (2011–  
559 2020; **Fig. 3a, 3b**) also shows persistent high AOD values in the IGP and its outflow regions  
560 across all seasons. In PI, the presence of elevated mountain ranges such as the Western and  
561 Eastern Ghats, coupled with its proximity to the Indian Ocean, results in regional-scale AOD  
562 variability. During the pre-monsoon and monsoon periods, oceanic and coastal regions  
563 exhibit higher AOD levels compared to the winter and post-monsoon periods. Though  
564 dominant spatial patterns are same in long term AOD from spaceborne sensors and their  
565 differences with ground-based AOD over same spatial grids are minimal (**Figs. S7a, b**), the  
566 discrepancy persists, especially over northern India and during monsoon period. As cloud-  
567 haze misclassifications may act as one of the factors from the observed differences between  
568 satellite and ground AOD in the monsoon periods, haze-removal criteria (following Jiao et  
569 al., 2023) to MODIS AOD was applied. A significant impact of haze over the peninsular  
570 region is seen during monsoon (Supplementary **Figs. S7c, d**), however, it shows negligible  
571 influence during the other seasons. This is clearly seen from the difference maps between the  
572 MODIS and ground-AOD over different ground locations, showing minimal changes before  
573 and after the haze removal. This exercise suggests that cloud-haze misclassification is not the  
574 primary factor driving the observed differences, except under monsoon conditions. Under  
575 such a scenario, localized discrepancies may arise due to spatial sampling limitations of the  
576 ground- based observations. As the ARFINET stations are sparsely and unevenly distributed,  
577 particularly across regions of high aerosol loading in northern India, this may result in the  
578 apparent lack of complete regional representation of ground observations. Additionally,  
579 discrepancies between MODIS and MISR AOD are also seen owing to fixed and multi angle  
580 retrievals especially in Pre-monsoon period over the NW region, where MISR AOD is  
581 significantly different from MODIS. There are also some pockets where low AOD region  
582 observed by MODIS is alternatively represented as a region of higher AOD in MISR  
583 observations, particularly in proximity to the IGP outflow. Previous studies over similar  
584 geographic regions have indicated that the frequency of observations, cloud masking, and  
585 geographical factors impact both MODIS and MISR observations, stemming from algorithm  
586 assumptions related to cloud masking and SSA. Overall, the spatial patterns of AOD from  
587 ground and satellite observations reveal the following:

- 588 • During the pre-monsoon period, northern India experiences increased AOD.
- 589 • During the winter season, cold temperatures, a low boundary layer height, and humid
- 590 air create hazy conditions with high AOD (Nair et al., 2020). Along with it, winds
- 591 over the IGP are mostly north-westerly, with an anti-cyclonic pattern over central
- 592 India, driving aerosols to peninsular region.
- 593 • The post-monsoon AOD also remains high, similar to winter levels, particularly in the
- 594 IGP due to biomass burning (Kumar et al., 2012; Lodhi et al., 2013; Subba et al.,
- 595 2021).
- 596 • The spatial patterns of AOD across different seasons are well captured by both
- 597 satellite and ground-based observations. However, notable differences exist between
- 598 ground-based and MODIS and MISR AOD. While MODIS tends to overestimate
- 599 AOD over the IGP, it generally underestimates AOD over the PI, NE, and NW
- 600 regions. MISR significantly underestimates higher AOD regions.

601 *Despite the above constraints, the general agreement in magnitude and temporal variability*  
 602 *supports the reliability of both datasets for the fusion framework. Thus, our approach*  
 603 *explicitly accounts for such discrepancies by integrating the broad spatial coverage of satellite*  
 604 *observations with the higher accuracy of ground-based measurements. In this context, ground*  
 605 *observations are treated as local constraints rather than complete spatial representations,*  
 606 *thereby minimizing the influence of regional sampling gaps in the ground network.*  
 607 *Consequently, the final fused AOD represents a bias-corrected satellite-derived field*  
 608 *constrained by ground observations.*



609 **Figure 3a.** Long-term (2011-2020) satellite based AOD (at 550 nm) from MODIS over  
 610 south-Asian region.  
 611



612  
 613 **Figure 3b.** Long-term (2011-2020) satellite based AOD (at 550 nm) from MISR over south-  
 614 Asian region.

615 **3.2 Inter-comparison of satellite- and ground-based AOD**

616 Having examined the spatial distribution, a quantitative evaluation of the associations or  
 617 biases between satellite and ground-based AOD at different periods is examined for the years  
 618 2012, 2016, and 2021. The three different years were selected such that way that the AOD for  
 619 2012 and 2021 provides the decadal variability, while 2016 represents an intermediate period  
 620 between these two years, enabling us to better assess the progression and variability of AOD  
 621 over a long period. The scatter plots (Supplementary **Figs. S8-S10**; the number of ground  
 622 stations included in the correlation studies is given in **Table 1**) between MODIS/ MISR and  
 623 ground-based AOD highlight moderate to strong correlations ( $\sim 0.8-0.9$ ) in winter (January)  
 624 and post-monsoon (November), while moderate correlations ( $\sim 0.54-0.77$ ) between the two  
 625 are observed in pre-monsoon (May). The RMSE between MISR and ground-based AOD is  
 626 higher ( $\geq 0.2$ ) during winter and post-monsoon, whereas higher RMSE values between  
 627 MODIS and ground-based AOD are observed during the pre-monsoon period. The prominent  
 628 locations contributing to mean errors and weak correlations with ground observations are  
 629 situated in the NW and IGP regions.

630 The quartile-plots (**Figs. S11-S13**) highlight significant spatio-temporal variability in AOD,  
 631 with both sensors displaying higher AOD over terrestrial regions, particularly in the IGP, its  
 632 outflows, and South (Peninsular) and Central India. The third and fourth quartiles are more  
 633 representative for AOD over land regions than in surrounding areas like oceans and elevated  
 634 terrain. Data with respect to longitude and latitude show that higher AOD values are mostly  
 635 confined to  $20^{\circ}-30^{\circ}\text{N}$  latitude and  $80^{\circ}-95^{\circ}\text{E}$  longitude. However, MODIS consistently  
 636 recorded significantly higher AOD values than MISR, with notable dissimilarities in quartile  
 637 patterns over northern India during May.

638 Both the correlation and quartile analyses highlight the advantages and limitations of MODIS  
639 and MISR observations. For example, MISR tends to underestimate high AOD conditions in  
640 urban regions compared to MODIS, even though it can effectively separate surface  
641 contributions under low aerosol loading, as also reported by Tao et al. (2020). Under high  
642 AOD conditions, the benefit of multi-angle measurements becomes limited, as thick aerosol  
643 layers smooth out surface reflectance signals (BRDF), potentially leading to an  
644 underestimation of AOD due to misattribution of aerosol contributions to surface reflectance.  
645 In contrast, when dust loading is dominated by coarse and non-spherical particles (in May),  
646 MISR demonstrates relatively better performance than MODIS (as shown by scatter plots).  
647 This difference may be attributed to the advantage of MISR's multi-angle observation  
648 capability, consistent with findings from Middle Eastern validation studies (Farahat, 2019;  
649 Garay et al., 2017).

650 **Table 1:** Number of ground stations data used in different months of the year 2012, 2016, and  
651 2021.

2012	2016	2021	2012	2016	2021	2012	2016	2021
Jan	Jan	Jan	May	May	May	Nov	Nov	Nov
21	26	16	22	25	13	27	26	16

### 652 3.3 Fusion of satellite- and ground-based AOD

#### 653 3.3.1 Variogram analysis

654 For the fusion of satellite- and ground-based AOD, the experimental variogram (using eq.2) is  
655 first obtained from the gridded satellite data. As mentioned in section 2.3.2, a well-fitted  
656 variogram is essential for determining appropriate parameters in geographical processes.  
657 These variogram parameters like sill, range, and nugget are not unique but depend on the  
658 theoretical models used. The choice of fitting is determined through a least square approach,  
659 selecting the best fit based on the least sum of squared errors (SSE). However, the availability  
660 of a large number of satellite data sets has made this task easier. The variogram depicted in  
661 supplementary **Figs. S14, S15, and S16** demonstrate a flattening of variance after a certain  
662 lag (interval between distances), affirming the effectiveness of our implemented detrending  
663 method. AOD values within the range highlight spatial correlation, wherein the correlated  
664 AOD values are influential in determining missing AOD values. The variogram parameters  
665 obtained from the fitted theoretical model are given in **Tables 2 and 3**.

666 The variogram parameters corresponding to different sensors exhibit noticeable variation  
667 across months and years, reflecting differences in their retrieval characteristics and ability to  
668 represent AOD. For instance, both MODIS and MISR show shorter spatial correlation lengths  
669 in May compared to January and November. Such reduced ranges are typically associated  
670 with long-range dust or smoke transport processes, which dominate during this period in the  
671 study region. Conversely, longer ranges indicate that the sensor retrievals capture more  
672 spatially homogeneous values, suggesting an improved ability to represent regional  
673 heterogeneity. In this study, we prioritize MODIS variograms because of their higher sill and  
674 range values, which demonstrate stronger spatial dependency (Isaaks, 1991; Vieira et al.,  
675 2009). Nevertheless, sensitivity tests indicate that using variograms derived from either  
676 MODIS or MISR produces only negligible differences ( $\sim 0.01$ ) in the fused AOD estimates.  
677 (**Fig. S17**). At this stage, it is also to be noted that geographically weighted or local variogram

678 approaches can better represent spatial heterogeneity, particularly over complex terrains such  
679 as the Himalayas and Western Ghats. However, in the present study, this approach was not  
680 feasible due to the limited availability of ground-based AOD observations, especially across  
681 high-altitude regions. The sparse coverage restricts the stability and generalizability of local  
682 variogram fitting, particularly at regional boundaries where different models would be  
683 required. For this reason, we adopted a single variogram model, following the approach used  
684 for large regions (e.g., eastern and western USA; Chatterjee et al. (2010)), which provides a  
685 more consistent framework for regional-scale fusion).

686 **Table 2:** Parameters obtained from variogram in different seasons (January, May, and  
687 November) of different years (2012, 2016, and 2021) from MODIS.

Year	Month	MODEL	Nugget	sill	Range (in km)
2012	Jan	Matheron	0	0.033954	848.5
2016	Jan	Exponential	0.000015	0.057399	453.3
2021	Jan	Exponential	0	0.052327	854.0
2012	May	Matheron	0	0.026499	555.6
2016	May	Matheron	0	0.029704	489.1
2021	May	Matheron	0	0.034273	378.3
2012	Nov	Matheron	0	0.030027	548.3
2016	Nov	Spherical	0	0.029582	1080.7
2021	Nov	Exponential	0	0.040153	696.2

688 **Table 3:** Parameters obtained from variogram in different seasons (January, May, and  
689 November) of different years (2012, 2016, and 2021) from MISR.

Year	Month	MODEL	Nugget	sill	Range (in km)
2012	Jan	Exponential	0.000062	0.011589	645.6
2016	Jan	Spherical	0.000177	0.017749	1060.6
2021	Jan	Matheron	0	0.027958	927.9
2012	May	Matheron	0	0.016100	371.1
2016	May	Exponential	0.001741	0.018171	463.0
2021	May	Matheron	0.000833	0.017896	533.5
2012	Nov	Exponential	0.000022	0.014509	638.7
2016	Nov	Matheron	0	0.018378	583.0
2021	Nov	Matheron	0.0000925	0.019104	516.4

### 690 3.3.2 Spatial interpolation of AOD

691 Monthly mean AOD gives the advantage of having full regional picture of columnar aerosol  
692 load over south-Asian region. However, it is observed that both MODIS and MISR AOD  
693 show gaps in some of the regions, either due to consistent cloud coverage or due to complex  
694 orography coupled with highly reflective land masses (e.g., snow-covered regions of the  
695 Himalayas). Hence, UK with geographic parameters as regressors applied to fill these missing  
696 areas (which are found to be  $\sim 2-11\%$ ) to obtain a complete spatial picture of AOD over the  
697 south-Asian region. Since kriging gives a probability map, the associated variance is higher in

698 the gap regions than in the regions where values exist. Thus, the interpolated values and  
699 variances are not unique, as they depend on the variogram and trend models used in the  
700 interpolation. On the other hand, the variogram can have uncertainties that stem from factors  
701 such as lag spacing, the quantity of data points, and model fitting, as highlighted by  
702 researchers (Derakhshan and Leuangthong, 1982; Koushavand and Deutsch, 2008). Hence,  
703 our proposed approach is not intended solely to enhance spatial coverage, but to generate a  
704 bias-corrected and internally consistent AOD dataset through the optimal integration of  
705 complementary satellite products.

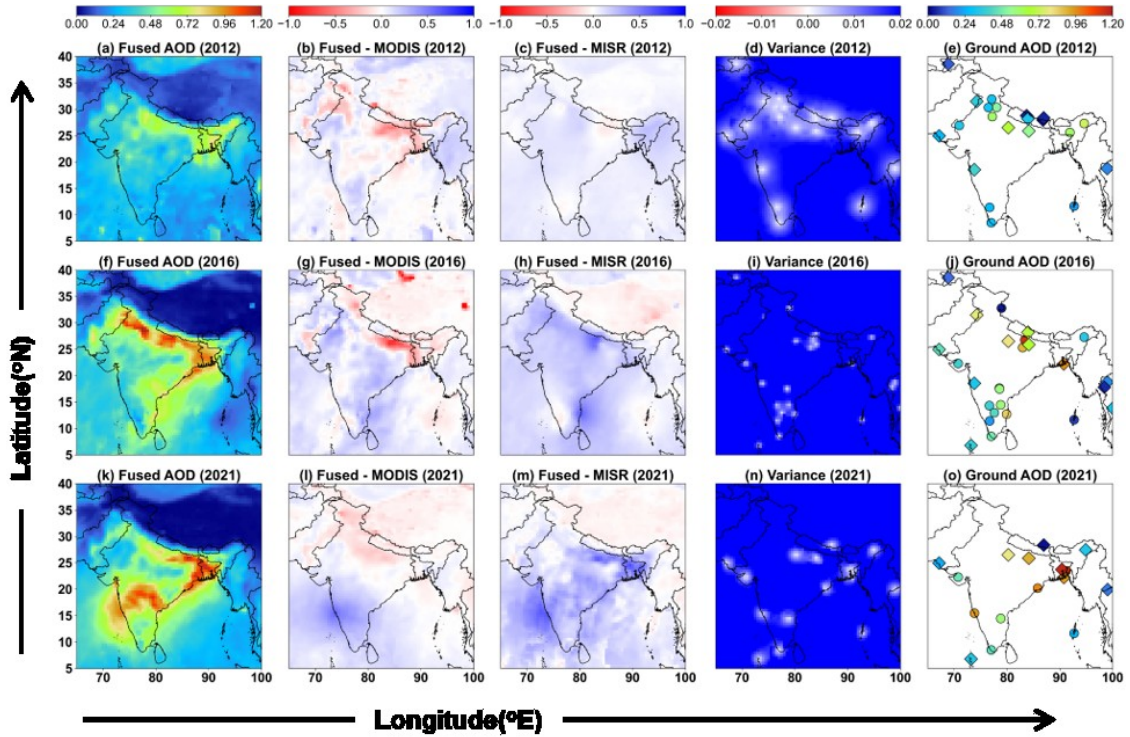
706 The spatial distribution of 0.5° gridded monthly mean raw and predicted (after spatial  
707 interpolation) AOD from MODIS and MISR is shown in supplementary **Figs. S18-S23**. The  
708 performance metrics (in terms of R and RMSE) of this gap-filling approach are demonstrated  
709 through sensitivity studies, considering different spatial gaps in the data (**Fig. S24**). It is  
710 observed that the predicted AOD largely depends on the availability and spatial distribution  
711 of nearby observed data points. Regions such as the IGP, the Himalayan region, peninsular  
712 India, and oceanic areas generally show better performance, where smoother spatial gradients  
713 of AOD and more consistent regional aerosol patterns improve the reliability of the spatial  
714 predictions. Based on these sensitivity studies, the predicted AOD field appears to provide a  
715 reliable spatial representation with acceptable uncertainty as the interpolation (gap filling) is  
716 made over a relatively small fraction of missing values based on a large number of observed  
717 data points around the gap areas.

### 718 **3.3.3 Fused AOD**

719 The monthly fused AOD is generated using the UK fusion method, where satellite data are  
720 treated as trend model. This retains the overall spatial signatures of AOD from each satellite  
721 sensor. The optimal AOD values are determined by the weights obtained from spatial  
722 relationships, along with the trend of the satellite-based AOD at the estimation locations.  
723 **Figs. 4-6** show the fused maps of AOD at different seasons of the years 2012, 2016, and  
724 2021. The regional average values of fused AOD, along with AOD from individual sensors,  
725 are given in **Supplementary Tables ST4, ST5, and ST6**.

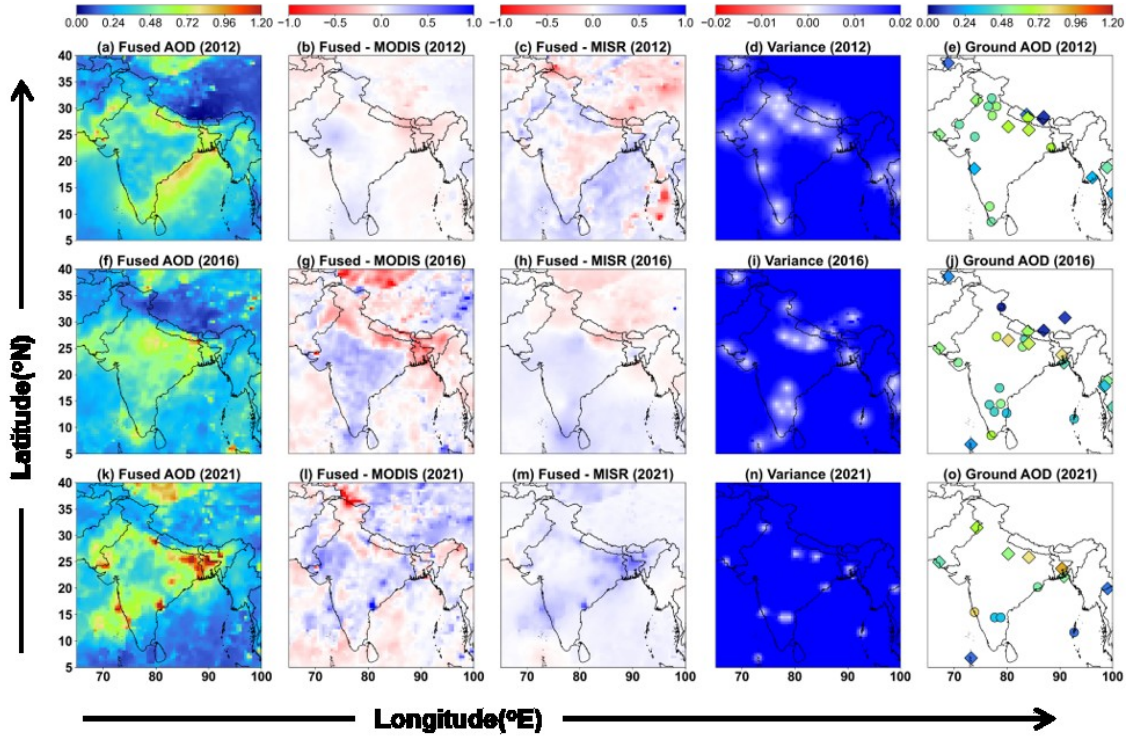
726 Throughout the observation period, the fusion maps highlight the significant influence of  
727 ground-based AOD on the fusion method. As shown in **Table 4**, the fused AOD is more  
728 aligned to ground-based AOD with a correlation (R)  $\sim 0.994-1$  and RMSE  $\sim 0.009-0.04$ . On  
729 the other hand, correlation between MODIS/MISR and fused AOD shows little improvement  
730 compared to that between MODIS/MISR and ground-based AOD (**Table 5a, b**). This  
731 indicates the robustness of the fusion approach keeping ground-based AOD as an anchoring  
732 reference.

733 The notable outcomes from fused AOD maps are the distinct spatial features compared to  
734 those obtained from individual space-based sensors. For example, during January 2016, the  
735 significant overestimation by MODIS (AOD  $\sim 1.7$ ) relative to ground-based AOD ( $\sim 1.2$ ) is  
736 adjusted in the fused AOD distribution, thus correcting the bias but maintaining the spatial  
737 heterogeneity. Similarly, in Jan 2021, MODIS and MISR significantly underestimated AOD  
738 over peninsular India (MODIS AOD  $\sim 0.36$  and MISR AOD  $\sim 0.30$ ) as compared to ground  
739 AOD (e.g., AOD at GOA  $\sim 0.95$ ). The fused AOD corrects this bias toward values closer to  
740 ground-based observations, retaining continuous flow of aerosols toward the Arabian coast.



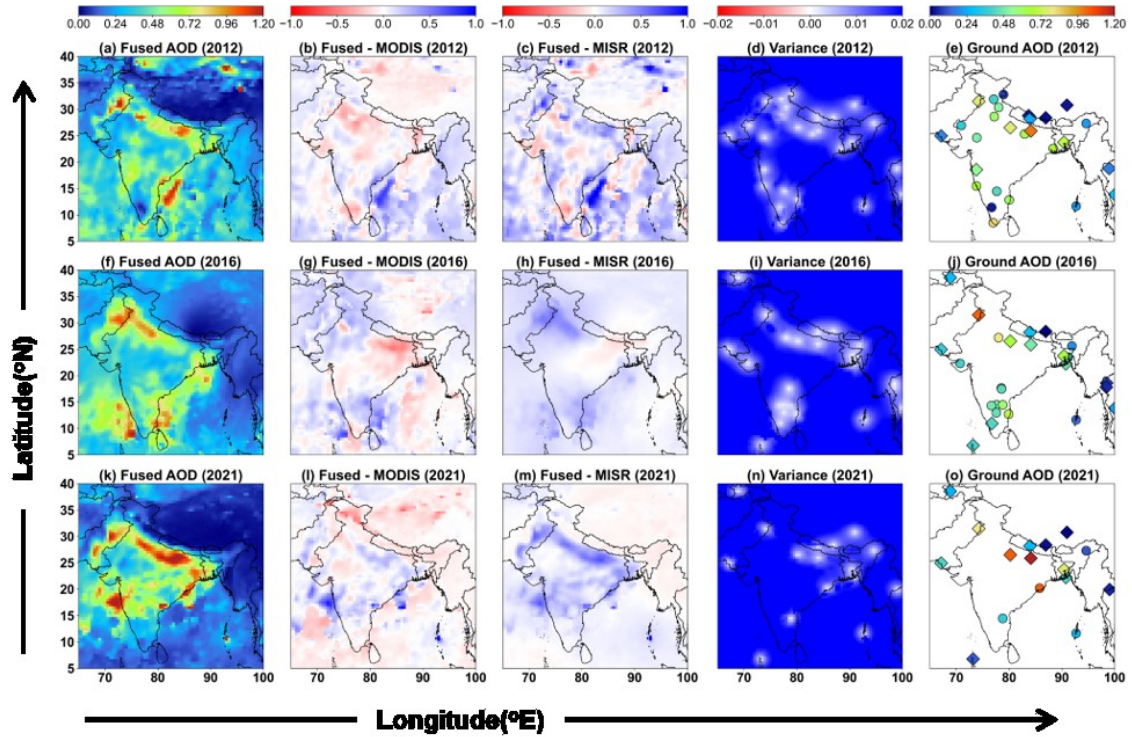
741

742 **Figure 4.** Monthly fused AOD (at 550 nm) maps [(a), (f) and (k)] in January for the years  
 743 2012, 2016, 2021; [(b), (g) and (i)] and [(c), (h) and (m)] - the deviations of fused AOD from  
 744 corresponding sensors, i.e., MODIS and MISR; [(d), (i) and (n)] variance; and [(e), (j) and  
 745 (o)] - ground-based AOD (ARFINET is represented by circle and AERONET by diamond  
 746 shapes) used to generate fused maps. Blue indicates overestimations, and red means an  
 747 underestimation of fused AOD from satellite retrieved AOD. The white dots in variance plots  
 748 show the ground station locations.



749

750 **Figure 5.** Similar analysis as in Fig. 4, but for the month of May in 2012, 2016, and 2021.



751

752 **Figure 6.** Similar analysis as in Fig. 4, but for the month of November in 2012, 2016, and  
 753 2021.

754 **Table 4:** Comparative analysis of fused vs ground –based AOD at ground station locations.

Year	Month	Fused & Ground				
		Correlation	RMSE	MAE	Slope	Bias
2012	Jan	0.998	0.014	0.011	1.024	0.003
	May	0.998	0.014	0.011	1.012	0.003
	Nov	0.996	0.025	0.017	1.026	0.004
2016	Jan	0.994	0.032	0.023	1.026	-0.006
	May	0.984	0.04	0.026	1.074	0.004
	Nov	0.994	0.026	0.018	0.994	-0.003
2021	Jan	0.999	0.022	0.015	1.03	0.008
	May	0.998	0.022	0.016	1.049	0.009
	Nov	1	0.009	0.007	1.003	0.002

755 Similar observations are also evident during the pre-monsoon period. However, during this  
 756 period, the fused maps retain more of MISR spatial patterns in 2016 and 2021, while  
 757 resembling MODIS in 2012. Notably, the discrepancies seen near coastal regions in May  
 758 (2021), particularly across the peninsular zone, may be attributed to higher cloud fractions  
 759 (Fig. S25), introducing greater uncertainty in aerosol-cloud discrimination (Lang et al., 2026),  
 760 thereby leading to inaccuracies in satellite-derived AOD estimate. Furthermore, AOD  
 761 retrievals in coastal areas may also be influenced by potential overestimation of boundary  
 762 layer height (BLH) in MODIS data (Wang et al., 2025a). The fused AOD, which primarily  
 763 incorporates the information from the availability and spatial proximity of ground-based  
 764 measurements, tends to show higher values in these regions, effectively correcting this bias  
 765 using ground-based observations.

766 **Table 5a:** Error and bias analysis of MODIS AOD with ground and fused AOD at ground  
 767 station locations.

Year	Month	MODIS & Ground					MODIS & Fused				
		Correlation	RMSE	MAE	Slope	Bias	Correlation	RMSE	MAE	Slope	Bias
2012	Jan	<b>0.781</b>	<b>0.144</b>	<b>0.106</b>	<b>0.858</b>	<b>0.074</b>	<b>0.789</b>	<b>0.142</b>	<b>0.105</b>	<b>0.896</b>	<b>0.067</b>
	May	0.770	0.128	<b>0.102</b>	0.704	0.147	0.788	0.122	0.096	0.732	0.137
	Nov	0.846	0.155	0.120	0.872	0.049	0.871	0.140	0.108	0.924	0.030
2016	Jan	0.792	0.250	0.164	1.096	-0.037	0.822	0.237	0.154	1.175	-0.083
	May	0.542	0.269	0.207	0.776	0.184	0.583	0.259	0.208	0.910	0.127
	Nov	0.773	0.157	0.121	0.759	0.064	0.787	0.153	0.115	0.774	0.055
2021	Jan	<b>0.861</b>	<b>0.199</b>	<b>0.138</b>	<b>0.911</b>	<b>0.010</b>	<b>0.879</b>	<b>0.185</b>	<b>0.127</b>	<b>0.958</b>	<b>-0.011</b>
	May	0.752	0.236	0.152	1.030	0.038	0.778	0.230	0.147	1.120	0.004
	Nov	<b>0.944</b>	<b>0.143</b>	<b>0.120</b>	<b>0.761</b>	<b>0.082</b>	<b>0.947</b>	<b>0.139</b>	<b>0.115</b>	<b>0.766</b>	<b>0.082</b>

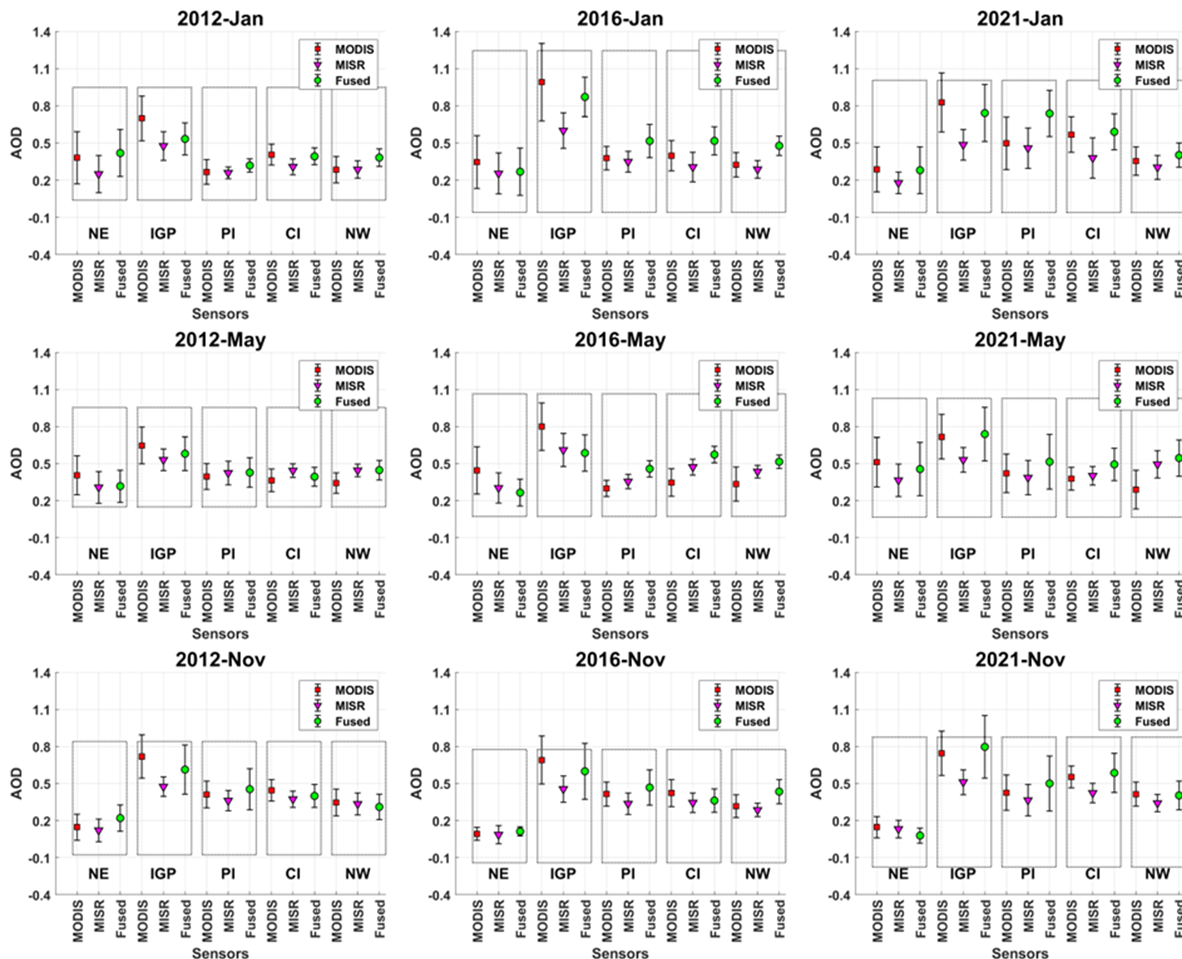
768 **Table 5b:** Error and bias analysis of MISR AOD with ground and fused AOD at ground  
 769 station locations.

Year	Month	MODIS & Ground					MODIS & Fused				
		Correlation	RMSE	MAE	Slope	Bias	Correlation	RMSE	MAE	Slope	Bias
2012	Jan	<b>0.884</b>	<b>0.115</b>	<b>0.090</b>	<b>0.676</b>	<b>0.049</b>	<b>0.897</b>	<b>0.106</b>	<b>0.082</b>	<b>0.704</b>	<b>0.042</b>
	May	0.643	0.159	<b>0.132</b>	0.437	0.189	0.656	0.154	0.129	0.452	0.184
	Nov	0.760	0.223	0.175	0.466	0.098	0.780	0.212	0.168	0.492	0.089
2016	Jan	0.783	0.270	0.206	0.421	0.010	0.818	0.263	0.203	0.454	0.081
	May	0.662	0.167	0.129	0.606	0.153	0.736	0.140	0.117	0.736	0.098
	Nov	0.814	0.186	0.143	0.515	0.079	0.834	0.185	0.144	0.528	0.072
2021	Jan	<b>0.824</b>	<b>0.346</b>	<b>0.267</b>	<b>0.372</b>	<b>0.131</b>	<b>0.838</b>	<b>0.332</b>	<b>0.258</b>	<b>0.390</b>	<b>0.123</b>
	May	0.772	0.205	0.160	0.458	0.147	0.805	0.185	0.147	0.502	0.130
	Nov	<b>0.944</b>	<b>0.251</b>	<b>0.186</b>	<b>0.492</b>	<b>0.092</b>	<b>0.948</b>	<b>0.248</b>	<b>0.182</b>	<b>0.495</b>	<b>0.091</b>

770 During the retreating monsoon season, the association of satellite and ground AOD is good,  
 771 with similar spatial distribution over northern regions, while significant differences exists  
 772 over southern parts. In the spatial map of fused AOD, the bias correction is clearly seen. In  
 773 November 2016, over the NW and IGP, a significant bias correction in satellite AOD is  
 774 observed, which is clearly indicated by the observed difference between fused AOD and  
 775 satellite measurements. Similarly, a flow pattern on the east coast of peninsular India is  
 776 corrected by fused AOD, which was otherwise underestimated by MISR (though retaining the  
 777 spatial pattern). Here, the fused map showed enhanced AOD attributed to observations from  
 778 ground stations, viz. Chennai (CHN) and Kadapa (KDP), which were underestimated by both  
 779 MODIS and MISR. Similarly, in November 2021, the flow over the IGP is modified in the  
 780 fused map based on ground observations

781 Over the IGP, where ground-based observations are more abundant than in other regions of  
 782 India, the regional mean fused AOD generally lies between MODIS and MISR values. This  
 783 reflects that the fusion process balances the biases between the tendency of MODIS to  
 784 overestimate and MISR to underestimate AOD in this region. In contrast, over Peninsular  
 785 India, which has the second-highest number of ground stations after the IGP, the fused AOD  
 786 is higher than both MODIS and MISR, suggesting that satellite based underestimation is  
 787 further adjusted in this region. Over northwest India during May, when dust loading is high,  
 788 the fused AOD is closer to MISR, consistent with previous studies showing that MISR  
 789 performs better than MODIS in dust-dominated regions due to its multi-angle capability.  
 790 However, over the NE, CI, and NW regions, the fused AOD remains higher than satellite

791 estimates. Fused AOD estimates over the Himalayas and oceanic regions are not analyzed in  
 792 detail due to the lack of sufficiently distributed ground-based observations. Overall, the fused  
 793 AOD is constrained locally on ground-based AOD, which are generally considered more  
 794 accurate than satellite-based observations whereas satellite retrievals exhibit discrepancies  
 795 due to variations in aerosol types and their source contributions, which likely explain the  
 796 observed differences in AOD estimates (Li et al., 2025; Wang et al., 2025b).



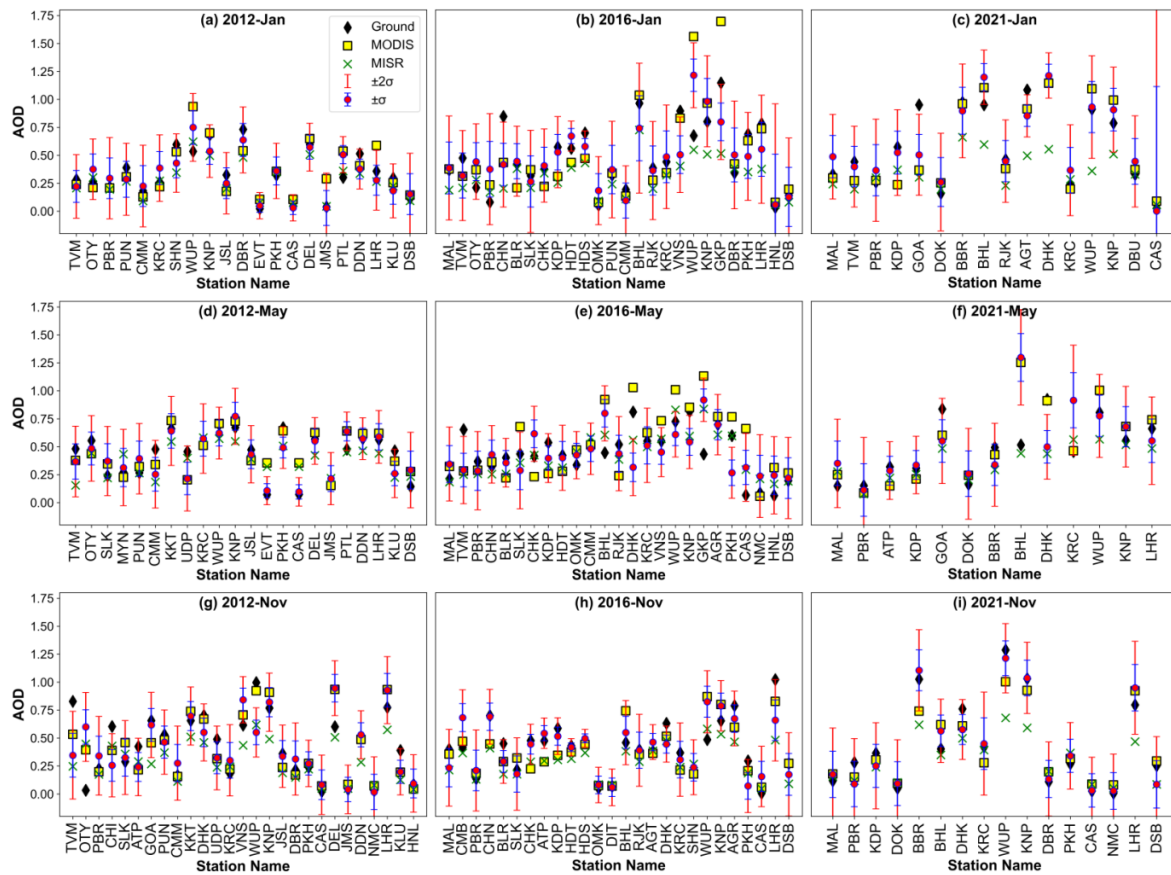
797  
 798 **Figure 7.** The regional mean values of MODIS, MISR, and fused AOD. On the y-axis, AOD  
 799 values are shown as mean  $\pm$  standard deviation.

800 With a view to assessing the improvement in the fused AOD estimates over MODIS and  
 801 MISR, further analysis is carried out on regional scale considering different sub-regions over  
 802 the study domain. **Fig. 7** shows the regional mean values of fused AOD along with AOD  
 803 from individual satellite sensors. It is observed that the fused AOD significantly improves the  
 804 biases in AOD from individual sensors. For example, in January 2012, MODIS AOD was  
 805 significantly higher than fused AOD over IGP, while MISR AOD was closer to fused AOD  
 806 over NE and CI regions. This indicates that the overestimation by MODIS in the IGP and the  
 807 underestimation by MISR in the NE and CI regions are effectively corrected by the fusion  
 808 framework. Similarly, in 2016, MODIS significantly overestimated AOD ( $\sim 0.99 \pm 0.31$ ) in  
 809 the IGP region. However, this was corrected in the fused AOD  $\sim 0.87 \pm 0.16$ , which also  
 810 closely matches ground-based AOD ( $\sim 0.86$ ). During the pre-monsoon period, MISR AOD  
 811 during 2012 and 2016 is closer to fused AOD; whereas in 2021, MODIS is closer to the fused  
 812 AOD over the NE, IGP, and PI regions than MISR, except over the CI and NW regions. This

813 behavior is consistent with the lower RMSE of MISR relative to ground-based AOD. Post-  
 814 monsoon analysis reveals MODIS AOD is closer to fused AOD over IGP with an  
 815 overestimation in 2012 and 2016, and an opposite pattern in 2021. MISR AOD is lower than  
 816 fused AOD in all these periods. These observations clearly indicate the regional level bias  
 817 corrections in the individual satellite sensors, resulting in a more accurate representation of  
 818 aerosol features in terms of fused AOD.

### 819 3.3.4 Performance analysis and cross-validation

820 The performance analysis carried out using the correlation analysis parameters such as RMSE  
 821 and MAE, revealed a decrease in RMSE and MAE in fused data and an increase in  
 822 correlation with MODIS and MISR (Figs S26-S28; Table 4, 5). However, the improvement  
 823 is inconsistent due to factors such as the variogram model used, errors between observation  
 824 values of ground observation, and MODIS, MISR. Thus, the final characteristics of fused  
 825 products are influenced by their individual instruments. The accuracy of fusion can be  
 826 concluded from the cross-validation analysis. This is characterized by LOOCV method.



827  
 828 **Figure 8.** Predicted AOD values (as magenta points) with error bars  $\pm\sigma$  (blue line),  $\pm 2\sigma$  (red  
 829 line), and ground observed AOD (black diamond), MODIS observation (yellow square),  
 830 MISR (green cross) at different stations. For station names refer **Table ST7 and ST8**.

831 **Figure 8** shows the predicted AOD values at each ground location during each leave-one-out  
 832 process. The prediction model performances analyzed in terms of mean prediction error  
 833 (MPE) and root mean square prediction error (RMSPE) are given in **Table 6**. The predicted  
 834 AOD values (as magenta points) at each of the ground locations with standard error bars  $\pm\sigma$   
 835 (blue line),  $\pm 2\sigma$  (grey line) are also shown in **Fig. 8**, along with AOD from the ground (black  
 836 diamond), MODIS (yellow triangle), MISR (red cross) observations. The figure shows that

837 more than 80% of ground AOD are within  $\pm 2\sigma$  (95% Confidence interval) of predicted AOD  
 838 for seven out of nine months. The highest accuracy was achieved in 2021 November and  
 839 2012 May (100%), and the lowest in 2016 May (76%), indicating the importance of the  
 840 association between different sensors during the fusion process. The enhanced accuracy of the  
 841 model for fused estimations required good correlation and reduced errors, as indicated in  
 842 **Tables 4, 5 & 6.**

843 **Table 6:** Accuracy assessment of the predicted AOD through leave-one-out cross-validation.  
 844 Here % describes how many ground AOD (actual values) are covered within the range of  
 845 predicted AOD.

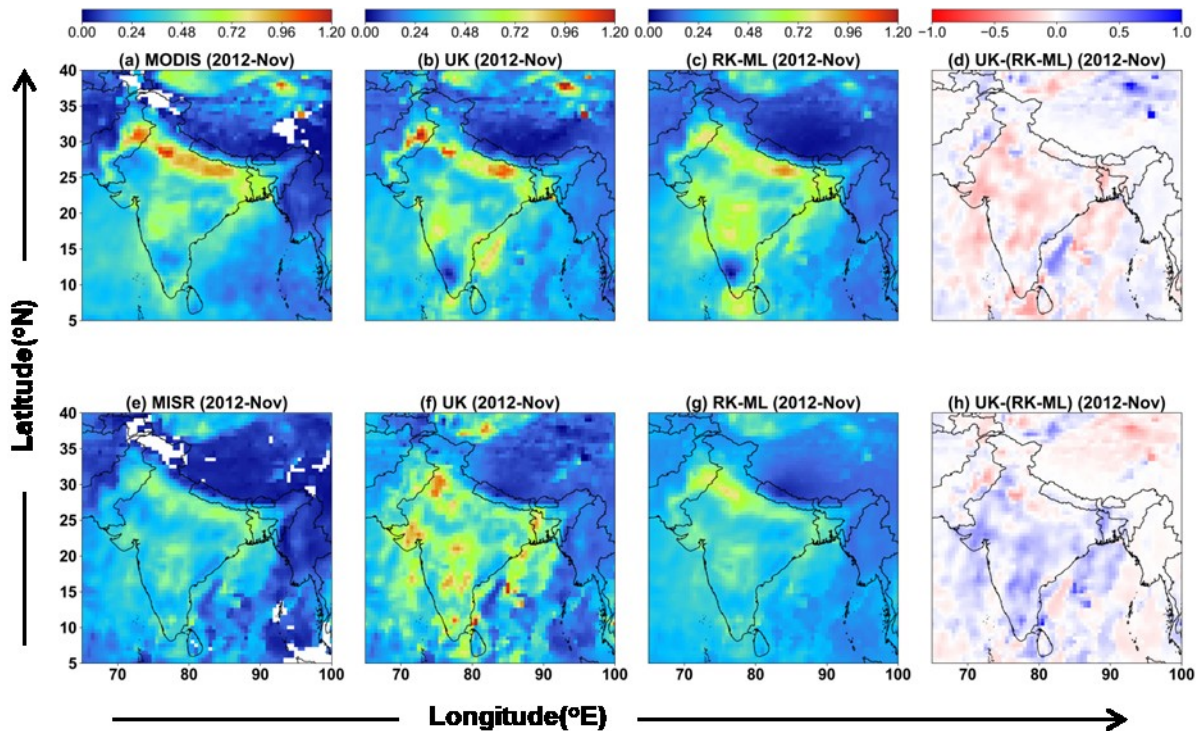
Year	Month	Correlation	RMSPE	MPE	Ground AOD within $\pm\sigma$ (in %)	Ground AOD within $\pm 2\sigma$ (in %)
2012	Jan	<b>0.852</b>	<b>0.108</b>	<b>0.091</b>	<b>76.19</b>	<b>95.24</b>
	May	<b>0.809</b>	<b>0.118</b>	<b>0.093</b>	<b>77.27</b>	<b>100</b>
	Nov	0.676	0.215	0.152	59.26	77.78
2016	Jan	0.708	0.213	0.160	65.38	84.62
	May	0.367	0.219	0.170	56	76
	Nov	0.793	0.146	0.109	65.38	88.46
2021	Jan	<b>0.893</b>	<b>0.162</b>	<b>0.121</b>	<b>81.25</b>	<b>81.25</b>
	May	0.451	0.302	0.212	61.54	84.62
	Nov	<b>0.964</b>	<b>0.108</b>	<b>0.086</b>	<b>87.50</b>	<b>100</b>

### 846 3.3.5 Machine Learning enhanced Geostatistical data fusion

847 To understand the influence of number of ground measurement points in the generation of  
 848 fused map, sensitivity studies has been carried out by varying the number of ground based  
 849 measurement points. The number of ground points from maximum of 27 ground locations has  
 850 been subsequently reduced to 22, 13, 8, and 6 respectively. The corresponding variations in  
 851 the fused outputs are provided (Supplementary **Fig. S29-S30, Table ST9**) and a special case  
 852 is included in **Fig. 9**. The figure clearly explains the changes in prevailing spatial pattern of  
 853 aerosols according to changes in number of data points, indicating that RK-ML method is a  
 854 good alternative to UK, when the available ground measurements are limited. This study also  
 855 indicates an inherent limitation in UK method, alike to multiple linear regression models,  
 856 which are highly susceptible to noise in predictor variables. In contrast, RK-ML demonstrates  
 857 greater robustness by first modeling the deterministic component using a machine learning  
 858 regressor (in this case, SVR), followed by kriging of the residuals to capture the stochastic  
 859 component. This two-step approach effectively leverages machine learning for optimized  
 860 estimation under noisy conditions, while kriging incorporates spatial variability of residuals  
 861 obtained from observations, resulting in more reliable spatial predictions.

862 Notably, when data points are fewer, UK has overestimated AOD values in mainland regions  
 863 relative to RK-ML predictions. This discrepancy may arise due to the complexity of the  
 864 underlying surface, where OK has been shown to outperform UK, as discussed on basis of  
 865 different surface types (Zimmerman et al., 1999). Since RK is an extension of OK, it inherits  
 866 these advantages, contributing to the improved performance of the RK-ML method. The  
 867 sensitivity study further highlights that variations in the number of ground station data points  
 868 and associated errors have a lesser impact on fused AOD from RK-ML approach in terms of  
 869 retaining spatial patterns compared to the UK-approach. This demonstrates the RK-ML  
 870 fusion ability to better manage observational uncertainties and data sparsely.

871

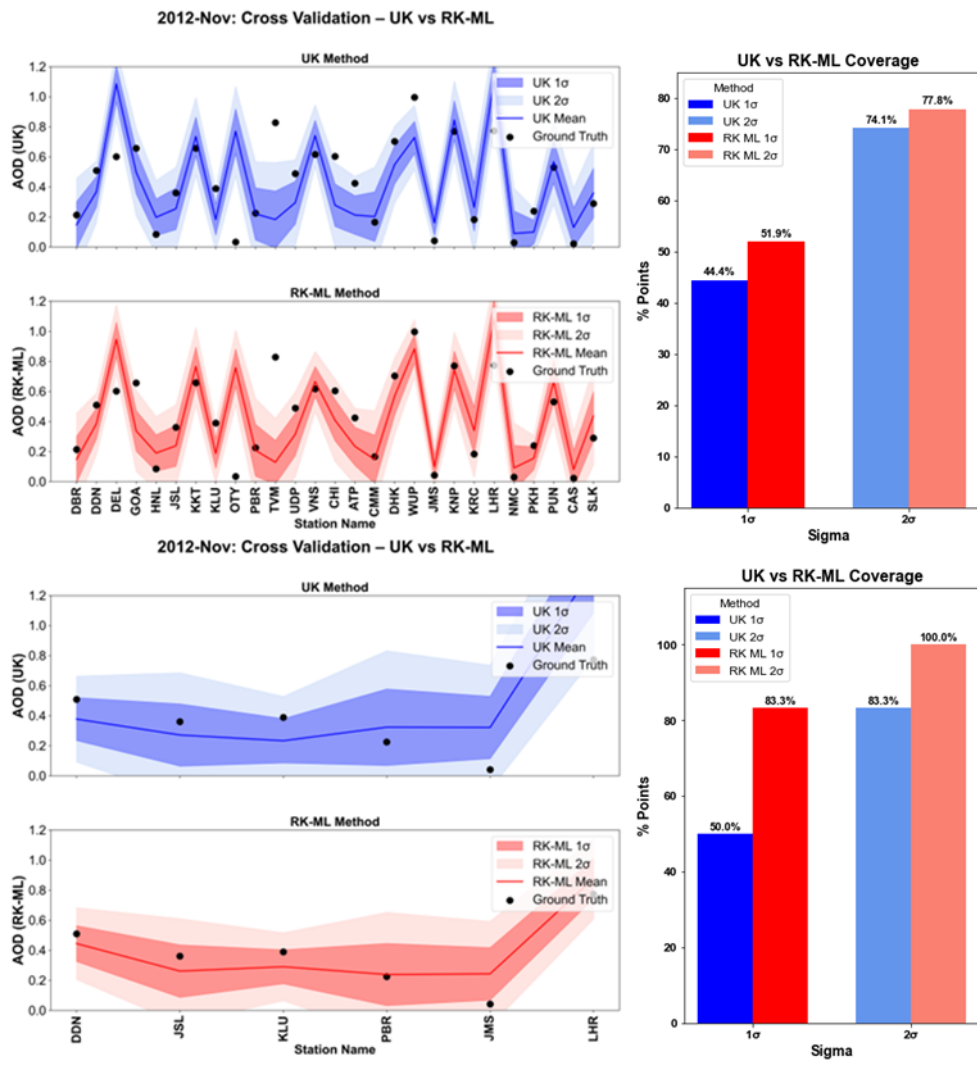


872  
 873 **Figure 9.** MODIS (a), MISR (e), and fused AOD using Universal Kriging (UK, (b), (f)), and  
 874 Residual Kriging with Machine Learning (RK-ML, (c), (g)); Difference between UK and RK-  
 875 ML predictions ((d), (h)). Blue color in difference map indicates where UK predictions  
 876 exceed those of RK-ML, and vice versa for red. The top panels (b, c and d) of fused AOD  
 877 shows estimations using 27 ground-data points (Case - 1), while the bottom panel (f, g and h)  
 878 shows fused AOD derived from 6 ground-data points (Case - 2).

879 The UK and RK-ML approach yields comparable results when the observations are higher in  
 880 number. On the other hand, RK-ML outperforms UK when the number of ground observation  
 881 is significantly decreased (**Fig. 10**). Hence, the accuracy of this estimation is significantly  
 882 influenced by the availability of small datasets, which indicates that the large number of  
 883 ground stations are crucial for best representation of fused AOD products from Universal  
 884 Kriging, while RK-ML is a good choice in case of limited number of ground observations.  
 885 Hence, the applicability of RK-ML can be made for generating fused AOD on daily basis per  
 886 each satellite overpasses over ground based stations.

887 The applicability of UK and RK-ML depends on their ability to capture realistic spatial  
 888 patterns from spatially representative data points (e.g., ground-based AOD) in order to  
 889 produce accurate fused AOD distributions. These estimations inherently carry uncertainties,  
 890 which increase with distance from ground observation sites. Consequently, the resulting maps  
 891 show elevated uncertainties in areas with sparse ground coverage. To evaluate model  
 892 performance under varying ground-station availability, we employed LOOCV. Results  
 893 indicate that RK-ML is generally more effective than UK when fewer ground observations  
 894 are available, as it can capture nonlinear relationships and penalize erroneous AOD values.  
 895 However, the Kriging step still requires a sufficient number of data points to propagate spatial  
 896 residuals. Similarly, UK applied with a limited number of stations (e.g., 27 in the present  
 897 study) estimates weights from collocated AOD points and satellite regressors (MODIS and  
 898 MISR). Thus, accurate uncertainty representation and improved fused AOD maps require a  
 899 more uniformly distributed network of ground stations. As illustrated in **Fig. S29**, increasing

900 station density enhances the similarity between fusion maps from both methods, as seen in the  
 901 larger white patches of the deviation plots (Fig. S29 a-d).



902  
 903 **Figure 10:** Line plots of LOOCV results from UK method (blue line) and RK-ML method  
 904 (red line), covering the ground AOD (black dots) for Case - 1 (27 points, 1<sup>st</sup> and 2<sup>nd</sup> line  
 905 plots) and case - 2 (6 points, 3<sup>rd</sup> and 4<sup>th</sup> line plots) within 1σ (dark shade) and 2σ (light  
 906 shade). For station names and details, refer to supplementary **Table ST8 and ST9**.

907 **4. Conclusion**

908 The utilization of a universal Kriging approach, combining satellite-based measurements with  
 909 ground-based observations, has demonstrated enhanced AOD estimation with reduced  
 910 uncertainties compared to relying on a single instrument. Despite inherent differences among  
 911 instruments, the implemented approach capitalizes on their complementary features,  
 912 statistically combining the three datasets to provide robust estimates. The significant  
 913 outcomes of this study are as follows:

- 914 • MODIS and MISR observations exhibit good but variable associations with ground-  
 915 based AOD measurements influenced by seasonal and geographic differences.
- 916 • Variogram analysis reveals different autocorrelation length implying capability of  
 917 each sensor to get the spatial variability or auto correlation structure in different  
 918 periods. In some of the months, MODIS shows higher spatial range as compared to

919 MISR, while the opposite is seen during the rest of the months. On the other hand, sill  
920 is always higher in case of MODIS.

- 921 • Spatial interpolation of AOD through variogram analysis provides very good  
922 predictions at the missing grids of the satellite observations, emphasizing the  
923 effectiveness of the universal Kriging method.
- 924 • The fused AOD maps reveal distinct results, highlighting the significant impact of  
925 ground-based AOD on the fusion process. During the pre-monsoon period  
926 specifically, the correlation coefficient and slope between MISR and fused AOD,  
927 which is comparable to ground-based AOD at point locations, improved by ~11% and  
928 ~21%, respectively. Furthermore, the RMSE was reduced by ~16% compared to pre-  
929 fusion values. These results demonstrate a marked improvement in the spatial  
930 representation of ground AOD following the fusion process. Additionally, the near-  
931 perfect correlation ( $R \sim 0.99$ ) between fused and ground-based AOD suggests effective  
932 bias correction in MODIS or MISR datasets, which otherwise significantly  
933 overestimated or underestimated aerosol measurements across certain parts of the  
934 study region.
- 935 • Cross-validation experiments further underline the effectiveness of the models in this  
936 study, e.g., strong correlations (0.964) and low RMSPE (0.108) and MPE (0.086)  
937 errors during November 2021. Even the model is able to predict 87.50 % of ground  
938 truths within  $\pm\sigma$  and even 100% within  $\pm 2\sigma$ . Moreover the measurements which were  
939 failed in predictions are due to highly local heterogeneity influenced by nearby ground  
940 measurements only.
- 941 • Incorporating a greater number of ground-based measurements enhances the fused  
942 results, yielding a cross-validation accuracy ranging from approximately 78% to 88%  
943 (based on 27 ground location points in November 2012 and 26 points in November  
944 2016). However, the alternative RK-ML method can also be effective when long-term  
945 observation stations are available, even if their numbers are limited. The establishment  
946 of additional ground-based stations is recommended to strengthen the representation  
947 of air quality, especially in regions with high heterogeneity. This methodology can be  
948 implemented to get the fusion maps of finer spatiotemporal resolution.

#### 949 **Author Contributions Statement:**

950 **SSG** - Data Curation, Software, Formal analysis, Visualization, Investigation, Writing -  
951 Original Draft and Editing; **MMG** - Methodology, Visualization, Validation, Software,  
952 Writing, Review and Editing, Supervision; **SSB** - Conceptualization, Supervision, Review  
953 and Editing, Project administration.

#### 954 **Acknowledgments:**

955 This study was carried out as part of the ARFI project of ISRO-GBP. We express our sincere  
956 thanks to the ARFINET investigators for the continued support and long-term contributions  
957 over the years in operating the network. We authors are also thankful to the AERONET team  
958 for providing AOD data (data available at <http://aeronet.gsfc.nasa.gov>). Additionally, we  
959 acknowledge NASA's Level-1 and Atmosphere Archive and Distribution System Distributed  
960 Active Archive Center (LAADS DAAC) and the Atmospheric Science Data Center (ASDC)  
961 for making the MODIS and MISR datasets available.

962 **References:**

- 963 Babu, S. S., Krishna Moorthy, K., and Satheesh, S. K.: Temporal heterogeneity in aerosol  
964 characteristics and the resulting radiative impacts at a tropical coastal station – Part 2:  
965 Direct short wave radiative forcing, *Ann. Geophys.*, 25, 2309–2320,  
966 <https://doi.org/10.5194/angeo-25-2309-2007>, 2007.
- 967 Bai, K., Li, K., Shao, L., Li, X., Liu, C., Li, Z., and Ma, M.: LGHAP v2 : a global gap-free  
968 aerosol optical depth and PM<sub>2.5</sub> concentration dataset since 2000 derived via big  
969 Earth data analytics, 2425–2448, 2024.
- 970 Baisad, K., Chutsagulprom, N., and Moonchai, S.: A Non-Linear Trend Function for Kriging  
971 with External Drift Using Least Squares Support Vector Regression, *Mathematics*, 11,  
972 4799, <https://doi.org/10.3390/math11234799>, 2023.
- 973 Basart, S., Pérez, C., Cuevas, E., Baldasano, J. M., and Gobbi, G. P.: Aerosol characterization  
974 in Northern Africa, Northeastern Atlantic, mediterranean basin and middle east from  
975 direct-sun AERONET observations, *Atmos. Chem. Phys.*, 9, 8265–8282,  
976 <https://doi.org/10.5194/acp-9-8265-2009>, 2009.
- 977 Brereton, R. G. and Lloyd, G. R.: Support Vector Machines for classification and regression,  
978 *Analyst*, 135, 230–267, <https://doi.org/10.1039/b918972f>, 2010.
- 979 Chatterjee, A., Michalak, A. M., Kahn, R. A., Paradise, S. R., Braverman, A. J., and Miller,  
980 C. E.: A geostatistical data fusion technique for merging remote sensing and ground-  
981 based observations of aerosol optical thickness, *J. Geophys. Res. Atmos.*, 115, 1–12,  
982 <https://doi.org/10.1029/2009JD013765>, 2010.
- 983 Chen, Z.-Y., Jin, J.-Q., Zhang, R., Zhang, T.-H., Chen, J.-J., Yang, J., Ou, C.-Q., and Guo,  
984 Y.: Comparison of Different Missing-Imputation Methods for MAIAC (Multiangle  
985 Implementation of Atmospheric Correction) AOD in Estimating Daily PM<sub>2.5</sub> Levels,  
986 *Remote Sens.*, 12, <https://doi.org/10.3390/rs12183008>, 2020.
- 987 Chu, D. A., Kaufman, Y. J., Ichoku, C., Remer, L. A., Tanré, D., and Holben, B. N.:  
988 Validation of MODIS aerosol optical depth retrieval over land, *Geophys. Res. Lett.*, 29,  
989 MOD2-1-MOD2-4, <https://doi.org/10.1029/2001GL013205>, 2002.
- 990 Chua, S. H. and Bras, R. L.: Optimal estimators of mean areal precipitation in regions of  
991 orographic influence, *J. Hydrol.*, 57, 23–48, [https://doi.org/10.1016/0022-1694\(82\)90101-9](https://doi.org/10.1016/0022-1694(82)90101-9), 1982.
- 993 Derakhshan, H. and Leuangthong, O.: Impact of Data Spacing on Variogram Uncertainty, 1–  
994 19, 1982.
- 995 Eck, T. F., Holben, B. N., Reid, J. S., Dubovik, O., Smirnov, A., O’Neill, N. T., Slutsker, I.,  
996 and Kinne, S.: Wavelength dependence of the optical depth of biomass burning, urban,  
997 and desert dust aerosols, <https://doi.org/10.1029/1999JD900923>, 1999.
- 998 Edward H. Isaaks, R. M. S.: An Introduction to Applied Geostatistics, *Comput. Geosci.*, 17,  
999 471–473, [https://doi.org/10.1016/0098-3004\(91\)90055-I](https://doi.org/10.1016/0098-3004(91)90055-I), 1991.
- 1000 Farahat, A.: Comparative analysis of MODIS, MISR, and AERONET climatology over the  
1001 Middle East and North Africa, *Ann. Geophys.*, 37, 49–64,  
1002 <https://doi.org/10.5194/angeo-37-49-2019>, 2019.
- 1003 Filonchyk, M., Yan, H., Zhang, Z., Yang, S., Li, W., and Li, Y.: Combined use of satellite  
1004 and surface observations to study aerosol optical depth in different regions of China,  
1005 *Sci. Rep.*, 9, 1–15, <https://doi.org/10.1038/s41598-019-42466-6>, 2019.
- 1006 Freier, L. and Von Lieres, E.: Kriging based iterative parameter estimation procedure for  
1007 biotechnology applications with nonlinear trend functions, *IFAC-PapersOnLine*, 28,  
1008 574–579, <https://doi.org/10.1016/j.ifacol.2015.05.043>, 2015.
- 1009 Freier, L., Wiechert, W., and von Lieres, E.: Kriging with trend functions nonlinear in their  
1010 parameters: Theory and application in enzyme kinetics, *Eng. Life Sci.*, 17, 916–922,  
1011 <https://doi.org/10.1002/elsc.201700022>, 2017.
- 1012 Gao, L., Chen, L., Li, C., Li, J., Che, H., and Zhang, Y.: Evaluation and possible uncertainty

1013 source analysis of JAXA Himawari-8 aerosol optical depth product over China, *Atmos.*  
1014 *Res.*, 248, 105248, <https://doi.org/10.1016/j.atmosres.2020.105248>, 2021.

1015 Garay, M. J., Kalashnikova, O. V., and Bull, M. A.: Development and assessment of a higher-  
1016 spatial-resolution (4.4 km) MISR aerosol optical depth product using AERONET-  
1017 DRAGON data, *Atmos. Chem. Phys.*, 17, 5095–5106, [https://doi.org/10.5194/acp-17-](https://doi.org/10.5194/acp-17-5095-2017)  
1018 5095-2017, 2017.

1019 Giles, D. M., Sinyuk, A., Sorokin, M. G., Schafer, J. S., Smirnov, A., Slutsker, I., Eck, T. F.,  
1020 Holben, B. N., Lewis, J. R., Campbell, J. R., Welton, E. J., Korokin, S. V., and  
1021 Lyapustin, A. I.: Advancements in the Aerosol Robotic Network (AERONET) Version  
1022 3 database - Automated near-real-time quality control algorithm with improved cloud  
1023 screening for Sun photometer aerosol optical depth (AOD) measurements, *Atmos.*  
1024 *Meas. Tech.*, 12, 169–209, <https://doi.org/10.5194/amt-12-169-2019>, 2019.

1025 Gogoi, M. M., Krishna Moorthy, K., Suresh Babu, S., and Bhuyan, P. K.: Climatology of  
1026 columnar aerosol properties and the influence of synoptic conditions: First-time results  
1027 from the northeastern region of India, *J. Geophys. Res. Atmos.*, 114,  
1028 <https://doi.org/10.1029/2008JD010765>, 2009.

1029 Guo, J., Gu, X., Yu, T., Cheng, T., Chen, H., and Xie, D.: Trend analysis of the aerosol  
1030 optical depth over China using fusion of MODIS and MISR aerosol products via  
1031 adaptive weighted estimate algorithm, *Earth Obs. Syst. XVIII*, 8866, 88661X,  
1032 <https://doi.org/10.1117/12.2024687>, 2013.

1033 Gupta, P., Patadia, F., and Christopher, S. A.: Multisensor data product fusion for aerosol  
1034 research, *IEEE Trans. Geosci. Remote Sens.*, 46, 1407–1415,  
1035 <https://doi.org/10.1109/TGRS.2008.916087>, 2008.

1036 Holben, B. N., Eck, T. F., Slutsker, I., Tanré, D., Buis, J. P., Setzer, A., Vermote, E., Reagan,  
1037 J. A., Kaufman, Y. J., Nakajima, T., Lavenu, F., Jankowiak, I., and Smirnov, A.:  
1038 AERONET - A federated instrument network and data archive for aerosol  
1039 characterization, *Remote Sens. Environ.*, 66, 1–16, [https://doi.org/10.1016/S0034-](https://doi.org/10.1016/S0034-4257(98)00031-5)  
1040 4257(98)00031-5, 1998.

1041 Holdaway, M. R.: Spatial modeling and interpolation of monthly temperature using kriging,  
1042 *Clim. Res.*, 6, 215–225, <https://doi.org/10.3354/cr006215>, 1996.

1043 Huang, J., Patrick Arnott, W., Barnard, J. C., and Holmes, H. A.: Theoretical uncertainty  
1044 analysis of satellite retrieved aerosol optical depth associated with surface albedo and  
1045 aerosol optical properties, *Remote Sens.*, 13, 1–21, <https://doi.org/10.3390/rs13030344>,  
1046 2021.

1047 Ichoku, C., Allen Chu, D., Mattoo, S., Kaufman, Y. J., Remer, L. A., Tanré, D., Slutsker, I.,  
1048 and Holben, B. N.: A spatio-temporal approach for global validation and analysis of  
1049 MODIS aerosol products, *Geophys. Res. Lett.*, 29, MOD1-1-MOD1-4,  
1050 <https://doi.org/10.1029/2001GL013206>, 2002.

1051 Jiang, X., Liu, Y., Yu, B., and Jiang, M.: Comparison of MISR aerosol optical thickness with  
1052 AERONET measurements in Beijing metropolitan area, *Remote Sens. Environ.*, 107,  
1053 45–53, <https://doi.org/10.1016/j.rse.2006.06.022>, 2007.

1054 Jiao, Y., Zhang, M., Wang, L., and Qin, W.: A New Cloud and Haze Mask Algorithm From  
1055 Radiative Transfer Simulations Coupled With, *IEEE Trans. Geosci. Remote Sens.*, 61,  
1056 1–16, <https://doi.org/10.1109/TGRS.2023.3252264>, 2023.

1057 Jin, S., Ma, Y., Li, H., Liu, B., Fan, R., Zhang, M., Lopatin, A., Dubovik, O., Hu, X., Gong,  
1058 W., and Wang, L.: Characterizing Aerosol Optical Properties and Direct Radiative  
1059 Effects From the Perspective of Components : A Synergy Retrieval Study Based on Sun  
1060 Photometer and Lidar in Central China, <https://doi.org/10.1029/2024GL113448>, 2025.

1061 Jinnagara Puttaswamy, S., Nguyen, H. M., Braverman, A., Hu, X., and Liu, Y.: Statistical  
1062 data fusion of multi-sensor AOD over the Continental United States, *Geocarto Int.*, 29,  
1063 48–64, <https://doi.org/10.1080/10106049.2013.827750>, 2014.

- 1064 Kadow, C., Hall, D. M., and Ulbrich, U.: Artificial intelligence reconstructs missing climate  
1065 information, *Nat. Geosci.*, 13, 408–413, <https://doi.org/10.1038/s41561-020-0582-5>,  
1066 2020.
- 1067 Kahn, R., Banerjee, P., and McDonald, D.: Sensitivity of multiangle imaging to natural  
1068 mixtures of aerosols over ocean, *J. Geophys. Res. Atmos.*, 106, 18219–18238,  
1069 <https://doi.org/10.1029/2000JD900497>, 2001.
- 1070 Kahn, R., Andrews, E., Brock, C. A., Chin, M., Feingold, G., Gettelman, A., Levy, R. C.,  
1071 Murphy, D. M., Nenes, A., Pierce, J. R., Popp, T., Redemann, J., Sayer, A. M., da Silva,  
1072 A. M., Sogacheva, L., and Stier, P.: Reducing Aerosol Forcing Uncertainty by  
1073 Combining Models With Satellite and Within-The-Atmosphere Observations: A Three-  
1074 Way Street, *Rev. Geophys.*, 61, 1–27, <https://doi.org/10.1029/2022rg000796>, 2023.
- 1075 Kalluri, R. O. R., Gugamsetty, B., Kotalo, R. G., Nagireddy, S. K. R., Tandule, C. R., Thotli,  
1076 L. R., Rajuru Ramakrishna, R., and Surendranair, S. B.: Direct radiative forcing  
1077 properties of atmospheric aerosols over semi-arid region, Anantapur in India, *Sci. Total*  
1078 *Environ.*, 566–567, 1002–1013, <https://doi.org/10.1016/j.scitotenv.2016.05.056>, 2016.
- 1079 Kim, M., Kim, J., Lim, H., Lee, S., Cho, Y., Lee, Y., Go, S., and Lee, K.: Aerosol optical  
1080 depth data fusion with Geostationary Korea Multi-Purpose Satellite ( GEO-KOMPSAT-  
1081 2 ) instruments GEMS , AMI , and GOCI-II: statistical and deep neural network  
1082 methods, 4317–4335, 2024.
- 1083 Kinne, S.: Remote sensing data combinations: superior global maps for aerosol optical depth,  
1084 *Satell. Aerosol Remote Sens. over L.*, 361–381, [https://doi.org/10.1007/978-3-540-69397-0\\_12](https://doi.org/10.1007/978-3-540-69397-0_12), 2009.
- 1086 Kompalli, S. K., Suresh Babu, S., and Krishna Moorthy, K.: Inter-comparison of aerosol  
1087 optical depth from the Multi-Wavelength Solar Radiometer with other radiometric  
1088 measurements, *Indian J. Radio Sp. Phys.*, 39, 364–371, 2010.
- 1089 Koushavand, B. and Deutsch, C. V: A Methodology to Quantify and Transfer Variogram  
1090 Uncertainty through Kriging and Simulation, *Cent. Comput. Geostatistics*, 1–16, 2008.
- 1091 Kumar, K. R., Narasimhulu, K., Reddy, R. R., Gopal, K. R., Reddy, L. S. S., Balakrishnaiah,  
1092 G., Moorthy, K. K., and Babu, S. S.: Temporal and spectral characteristics of aerosol  
1093 optical depths in a semi-arid region of southern India, *Sci. Total Environ.*, 407, 2673–  
1094 2688, <https://doi.org/10.1016/j.scitotenv.2008.10.028>, 2009.
- 1095 Kumar, S., Kumar, S., Singh, A. K., and Singh, R. P.: Seasonal variability of atmospheric  
1096 aerosol over the North Indian region during 2005-2009, *Adv. Sp. Res.*, 50, 1220–1230,  
1097 <https://doi.org/10.1016/j.asr.2012.06.022>, 2012.
- 1098 Lang, Q., Zhang, M., He, Q., Jin, S., Qin, W., Luo, L., and Wang, L.: Significant  
1099 uncertainties from overlooking aerosol-cloud coexistence in surface solar radiation  
1100 estimates using passive satellite observations, *Remote Sens. Environ.*, 333, 115168,  
1101 <https://doi.org/https://doi.org/10.1016/j.rse.2025.115168>, 2026.
- 1102 Levy, R. C., Remer, L. A., Martins, J. V, Kaufman, Y. J., Plana-Fattori, A., Redemann, J.,  
1103 and Wenny, B.: Evaluation of the MODIS Aerosol Retrievals over Ocean and Land  
1104 during CLAMS, 2005.
- 1105 Li, H., Zhang, M., Wang, L., Su, X., and Lu, Y.: Effects of Different Types of Aerosols on  
1106 Diffuse Radiation Based on Global AERONET, *J. Geophys. Res. Atmos.*, 130,  
1107 e2024JD042701, <https://doi.org/https://doi.org/10.1029/2024JD042701>, 2025.
- 1108 Li, J., Kahn, R. A., Wei, J., Carlson, B. E., Lacis, A. A., Li, Z., Li, X., Dubovik, O., and  
1109 Nakajima, T.: Synergy of Satellite- and Ground-Based Aerosol Optical Depth  
1110 Measurements Using an Ensemble Kalman Filter Approach, *J. Geophys. Res. Atmos.*,  
1111 125, 1–17, <https://doi.org/10.1029/2019JD031884>, 2020.
- 1112 Lilla, R. and Castrignanò, A.: Science of the Total Environment A geostatistical approach for  
1113 multi-source data fusion to predict water table depth Warning: Editor name is, *Sci.*  
1114 *Total Environ.*, 696, 133763, <https://doi.org/10.1016/j.scitotenv.2019.133763>, 2019.

- 1115 Litvinov, P., Chen, C., Dubovik, O., Zhai, S., Matar, C., Li, C., Lopatin, A., Fuertes, D.,  
 1116 Lapyonok, T., Bindreiter, L., Dornacher, M., Lehner, A., Dandocsi, A., Gasbarra, D.,  
 1117 and Retscher, C.: Synergetic retrieval from multi-mission spaceborne measurements for  
 1118 enhanced aerosol and surface characterization, 7679–7716, 2025.
- 1119 Liu, Y., Sarnat, J. A., Coull, B. A., Koutrakis, P., and Jacob, D. J.: Validation of Multiangle  
 1120 Imaging Spectroradiometer (MISR) aerosol optical thickness measurements using  
 1121 Aerosol Robotic Network (AERONET) observations over the contiguous United States,  
 1122 *J. Geophys. Res. Atmos.*, 109, <https://doi.org/10.1029/2003jd003981>, 2004.
- 1123 Lodhi, N. K., Beegum, S. N., Singh, S., and Kumar, K.: Aerosol climatology at Delhi in the  
 1124 western Indo-Gangetic Plain: Microphysics, long-term trends, and source strengths, *J.*  
 1125 *Geophys. Res. Atmos.*, 118, 1361–1375, <https://doi.org/10.1002/jgrd.50165>, 2013.
- 1126 Moorthy, K. K., Babu, S. S., Satheesh, S. K., Srinivasan, J., and Dutt, C. B. S.: Dust  
 1127 absorption over the “Great Indian Desert” inferred using ground-based and satellite  
 1128 remote sensing, *J. Geophys. Res. Atmos.*, 112, 1–10,  
 1129 <https://doi.org/10.1029/2006JD007690>, 2007.
- 1130 Moorthy K., K., Suresh Babu, S., and Satheesh, S. K.: Temporal heterogeneity in aerosol  
 1131 characteristics and the resulting radiative impact at a tropical coastal station – Part 1:  
 1132 Microphysical and optical properties, *Ann. Geophys.*, 25, 2293–2308,  
 1133 <https://doi.org/10.5194/angeo-25-2293-2007>, 2007.
- 1134 Nalder, I. A. and Wein, R. W.: Spatial interpolation of climatic Normals: Test of a new  
 1135 method in the Canadian boreal forest, *Agric. For. Meteorol.*, 92, 211–225,  
 1136 [https://doi.org/10.1016/S0168-1923\(98\)00102-6](https://doi.org/10.1016/S0168-1923(98)00102-6), 1998.
- 1137 Nguyen, H., Cressie, N., and Braverman, A.: Spatial statistical data fusion for remote sensing  
 1138 applications, *J. Am. Stat. Assoc.*, 107, 1004–1018,  
 1139 <https://doi.org/10.1080/01621459.2012.694717>, 2012.
- 1140 Nirala, M.: Multi-sensor data fusion of aerosol optical thickness, *Int. J. Remote Sens.*, 29,  
 1141 2127–2136, <https://doi.org/10.1080/01431160701395336>, 2008.
- 1142 Pathak, H. S., Satheesh, S. K., Nanjundiah, R. S., Moorthy, K. K., Lakshmiarahan, S., and  
 1143 Babu, S. N. S.: Assessment of regional aerosol radiative effects under the SWAAMI  
 1144 campaign - Part 1: Quality-enhanced estimation of columnar aerosol extinction and  
 1145 absorption over the Indian subcontinent, *Atmos. Chem. Phys.*, 19, 11865–11886,  
 1146 <https://doi.org/10.5194/acp-19-11865-2019>, 2019.
- 1147 Prasad, A. K. and Singh, R. P.: Comparison of MISR-MODIS aerosol optical depth over the  
 1148 Indo-Gangetic basin during the winter and summer seasons (2000-2005), *Remote Sens.*  
 1149 *Environ.*, 107, 109–119, <https://doi.org/10.1016/j.rse.2006.09.026>, 2007.
- 1150 Rossi, R. E., Dungan, J. L., and Beck, L. R.: Kriging in the shadows: Geostatistical  
 1151 interpolation for remote sensing, *Remote Sens. Environ.*, 49, 32–40,  
 1152 [https://doi.org/10.1016/0034-4257\(94\)90057-4](https://doi.org/10.1016/0034-4257(94)90057-4), 1994.
- 1153 Sayer, A. M., Hsu, N. C., Bettenhausen, C., and Jeong, M. J.: Validation and uncertainty  
 1154 estimates for MODIS Collection 6 “deep Blue” aerosol data, *J. Geophys. Res. Atmos.*,  
 1155 118, 7864–7872, <https://doi.org/10.1002/jgrd.50600>, 2013.
- 1156 Sayer, A. M., Munchak, L. A., Hsu, N. C., Levy, R. C., Bettenhausen, C., and Jeong, M.-J.:  
 1157 MODIS Collection 6 aerosol products: Comparison between Aqua’s e-Deep Blue, Dark  
 1158 Target, and “merged” data sets, and usage recommendations, *J. Geophys. Res. Atmos.*,  
 1159 119, 13,913-965,989, <https://doi.org/https://doi.org/10.1002/2014JD022453>, 2014.
- 1160 Sayer, A. M., Govaerts, Y., Kolmonen, P., Lipponen, A., Luffarelli, M., Mielonen, T.,  
 1161 Patadia, F., Popp, T., Povey, A. C., Stebel, K., and Witek, M. L.: A review and  
 1162 framework for the evaluation of pixel-level uncertainty estimates in satellite aerosol  
 1163 remote sensing, *Atmos. Meas. Tech.*, 13, 373–404, [https://doi.org/10.5194/amt-13-373-](https://doi.org/10.5194/amt-13-373-2020)  
 1164 2020, 2020.
- 1165 Schutgens, N., Sayer, A. M., Heckel, A., Hsu, C., Jethva, H., De Leeuw, G., Leonard, P. J. T.,

1166 Levy, R. C., Lipponen, A., Lyapustin, A., North, P., Popp, T., Poulsen, C., Sawyer, V.,  
1167 Sogacheva, L., Thomas, G., Torres, O., Wang, Y., Kinne, S., Schulz, M., Stier, P., and  
1168 Schutgens, N.: An AeroCom-AeroSat study: Intercomparison of satellite AOD datasets  
1169 for aerosol model evaluation, *Atmos. Chem. Phys.*, 20, 12431–12457,  
1170 <https://doi.org/10.5194/acp-20-12431-2020>, 2020.

1171 Sharma, V., Ghosh, S., Bilal, M., Dey, S., and Singh, S.: Performance of MODIS C6 . 1 Dark  
1172 Target and Deep Blue aerosol products in Delhi National Capital Region , India :  
1173 Application for aerosol studies, *Atmos. Pollut. Res.*, 12, 65–74,  
1174 <https://doi.org/10.1016/j.apr.2021.01.023>, 2021.

1175 Shaw, G. E., Reagan, J. A., and Herman, B. M.: Investigations of Atmospheric Extinction  
1176 Using Direct Solar Radiation Measurements Made with a Multiple Wavelength  
1177 Radiometer, *J. Appl. Meteorol.*, 12, 374–380, [https://doi.org/10.1175/1520-0450\(1973\)012<0374:IOAEUD>2.0.CO;2](https://doi.org/10.1175/1520-0450(1973)012<0374:IOAEUD>2.0.CO;2), 1973.

1179 Shi, Y., Li, L., and Zhang, L.: Application and comparing of IDW and Kriging interpolation  
1180 in spatial rainfall information, in: *Geoinformatics 2007: Geospatial Information  
1181 Science*, 67531I, <https://doi.org/10.1117/12.761859>, 2007.

1182 Sifaou, H., Kammoun, A., and Alouini, M. S.: A Precise Performance Analysis of Support  
1183 Vector Regression, *Proc. Mach. Learn. Res.*, 139, 9671–9680, 2021.

1184 Singh, M. K. and Venkatachalam, P.: Merging of aerosol optical depth data from multiple  
1185 remote sensing sensors, in: *2014 IEEE Geoscience and Remote Sensing Symposium*,  
1186 4173–4175, <https://doi.org/10.1109/IGARSS.2014.6947407>, 2014.

1187 Singh, M. K., Gautam, R., and Venkatachalam, P.: A merged aerosol dataset based on  
1188 MODIS and MISR Aerosol Optical Depth products, *Remote Sens. Atmos. Clouds,  
1189 Precip. VI*, 9876, 987627, <https://doi.org/10.1117/12.2223485>, 2016.

1190 Singh, P. and Verma, P.: A comparative study of spatial interpolation technique (IDW and  
1191 Kriging) for determining groundwater quality, in: *GIS and Geostatistical Techniques for  
1192 Groundwater Science*, Elsevier, 43–56, <https://doi.org/10.1016/B978-0-12-815413-7.00005-5>, 2019.

1194 Singh, P., Vaishya, A., Rastogi, S., and Babu, S. S.: Seasonal heterogeneity in aerosol optical  
1195 properties over the subtropical humid region of northern India, *J. Atmos. Solar-  
1196 Terrestrial Phys.*, 201, <https://doi.org/10.1016/j.jastp.2020.105246>, 2020.

1197 Sinha, P. R., Dumka, U. C., Manchanda, R. K., Kaskaoutis, D. G., Sreenivasan, S., Krishna  
1198 Moorthy, K., and Suresh Babu, S.: Contrasting aerosol characteristics and radiative  
1199 forcing over Hyderabad, India due to seasonal mesoscale and synoptic-scale processes,  
1200 *Q. J. R. Meteorol. Soc.*, 139, 434–450, <https://doi.org/10.1002/qj.1963>, 2013.

1201 Sivadasan Nair, V., Giorgi, F., and Keshav Hasyagar, U.: Amplification of South Asian haze  
1202 by water vapour-aerosol interactions, *Atmos. Chem. Phys.*, 20, 14457–14471,  
1203 <https://doi.org/10.5194/acp-20-14457-2020>, 2020.

1204 Smola, A. and Schölkopf, B.: A tutorial on support vector regression, *Stat. Comput.*, 14, 199–  
1205 222, <https://doi.org/10.1023/B%3ASTCO.0000035301.49549.88>, 2004.

1206 Snepvangers, J. J. J. C., Heuvelink, G. B. M., and Huisman, J. A.: Soil water content  
1207 interpolation using spatio-temporal kriging with external drift, *Geoderma*, 112, 253–  
1208 271, [https://doi.org/10.1016/S0016-7061\(02\)00310-5](https://doi.org/10.1016/S0016-7061(02)00310-5), 2003.

1209 Sogacheva, L., Popp, T., Sayer, A. M., Dubovik, O., Garay, M. J., Heckel, A., Christina Hsu,  
1210 N., Jethva, H., Kahn, R. A., Kolmonen, P., Kosmale, M., De Leeuw, G., Levy, R. C.,  
1211 Litvinov, P., Lyapustin, A., North, P., Torres, O., and Arola, A.: Merging regional and  
1212 global aerosol optical depth records from major available satellite products, *Atmos.  
1213 Chem. Phys.*, 20, 2031–2056, <https://doi.org/10.5194/acp-20-2031-2020>, 2020.

1214 Stein, A. and Corsten, L. C. A.: Universal Kriging and Cokriging as a Regression Procedure,  
1215 *Biometrics*, 47, 575, <https://doi.org/10.2307/2532147>, 1991.

1216 Subba, T., Gogoi, M. M., Moorthy, K. K., Bhuyan, P. K., Pathak, B., Guha, A., Srivastava,

1217 M. K., Vyas, B. M., Singh, K., Krishnan, J., Lakshmikumar, T. V. S., and Babu, S. S.:  
1218 Aerosol Radiative Effects Over India from Direct Radiation Measurements and Model  
1219 Estimates, *SSRN Electron. J.*, <https://doi.org/10.2139/ssrn.3986898>, 2021.

1220 Tandule, C. R., Gogoi, M. M., Gouda, S. S., and Suresh Babu, S.: Retrieval of aerosol optical  
1221 depth from INSAT-3DR for accurate geostationary monitoring of regional and temporal  
1222 aerosol dynamics, *Atmos. Environ.*, 367, 121730,  
1223 <https://doi.org/https://doi.org/10.1016/j.atmosenv.2025.121730>, 2026.

1224 Tang, Q., Bo, Y., and Zhu, Y.: Spatiotemporal fusion of multiple-satellite aerosol optical  
1225 depth (AOD) products using bayesian maximum entropy method, *J. Geophys. Res.*,  
1226 121, 4034–4048, <https://doi.org/10.1002/2015JD024571>, 2016.

1227 Tao, M., Wang, J., Li, R., Chen, L., Xu, X., Wang, L., Tao, J., Wang, Z., and Xiang, J.:  
1228 Characterization of Aerosol Type Over East Asia by 4.4 km MISR Product: First Insight  
1229 and General Performance, *J. Geophys. Res. Atmos.*, 125,  
1230 <https://doi.org/10.1029/2019JD031909>, 2020.

1231 Tao, M., Chen, J., Xu, X., Man, W., Xu, L., Wang, L., Wang, Y., Wang, J., Fan, M., Shahzad,  
1232 M. I., and Chen, L.: A robust and flexible satellite aerosol retrieval algorithm for multi-  
1233 angle polarimetric measurements with physics-informed deep learning method, *Remote  
1234 Sens. Environ.*, 297, 113763, <https://doi.org/https://doi.org/10.1016/j.rse.2023.113763>,  
1235 2023.

1236 Tian, X. and Gao, Z.: Validation and Accuracy Assessment of MODIS C6.1 Aerosol Products  
1237 over the Heavy Aerosol Loading Area, *Atmosphere (Basel)*, 10,  
1238 <https://doi.org/10.3390/atmos10090548>, 2019.

1239 Tian, X., Liu, Q., Li, X., and Wei, J.: Validation and comparison of MODIS C6.1 and C6  
1240 aerosol products over Beijing, China, *Remote Sens.*, 10,  
1241 <https://doi.org/10.3390/rs10122021>, 2018.

1242 Tiwari, S., Kaskaoutis, D., Soni, V. K., Dev Attri, S., and Singh, A. K.: Aerosol columnar  
1243 characteristics and their heterogeneous nature over Varanasi, in the central Ganges  
1244 valley, *Environ. Sci. Pollut. Res.*, 25, 24726–24745, [https://doi.org/10.1007/s11356-  
1245 018-2502-4](https://doi.org/10.1007/s11356-018-2502-4), 2018.

1246 Vieira, S., Carvalho, J., Ceddia, M., and Paz-González, A.: Detrending non stationary data for  
1247 geostatistical applications, *Bragantia*, 69, 1–8, [https://doi.org/10.1590/S0006-  
1248 87052010000500002](https://doi.org/10.1590/S0006-87052010000500002), 2009.

1249 Viswanatha Vachaspati, C., Reshma Begam, G., Nazeer Ahammed, Y., Raghavendra Kumar,  
1250 K., and Reddy, R. R.: Characterization of aerosol optical properties and model  
1251 computed radiative forcing over a semi-arid region, Kadapa in India, *Atmos. Res.*, 209,  
1252 36–49, <https://doi.org/10.1016/j.atmosres.2018.03.013>, 2018.

1253 Wang, H., Zhang, R., Liu, K., Wang, G., Liu, W., and Li, N.: Improved Kriging interpolation  
1254 based on support vector machine and its application in oceanic missing data recovery,  
1255 in: *Proceedings - International Conference on Computer Science and Software  
1256 Engineering, CSSE 2008*, 726–729, <https://doi.org/10.1109/CSSE.2008.924>, 2008.

1257 Wang, Y., You, Z., Wang, L., Wang, J., Zhou, M., Tao, M., and Kim, J.: First high temporal  
1258 resolution retrievals of AOD over shallow and turbid coastal waters for Himawari-8,  
1259 *ISPRS J. Photogramm. Remote Sens.*, 228, 603–612,  
1260 <https://doi.org/https://doi.org/10.1016/j.isprsjprs.2025.07.027>, 2025a.

1261 Wang, Z., Su, X., Wang, L., Lang, Q., Lu, Y., and Wang, L.: A Physics-Guided Neural  
1262 Network Model to Estimate All-Sky Diffuse Solar Radiation Using Himawari-8 Data,  
1263 *IEEE Trans. Geosci. Remote Sens.*, 63, 1–18,  
1264 <https://doi.org/10.1109/TGRS.2025.3543883>, 2025b.

1265 Wei, J., Li, Z., Sun, L., Peng, Y., and Wang, L.: Improved merge schemes for MODIS  
1266 Collection 6.1 Dark Target and Deep Blue combined aerosol products, *Atmos. Environ.*,  
1267 202, 315–327, <https://doi.org/10.1016/j.atmosenv.2019.01.016>, 2019.

- 1268 Witek, M. L., Garay, M. J., Diner, D. J., Bull, M. A., and Seidel, F. C.: New approach to the  
1269 retrieval of AOD and its uncertainty from MISR observations over dark water, *Atmos.*  
1270 *Meas. Tech.*, 11, 429–439, <https://doi.org/10.5194/amt-11-429-2018>, 2018.
- 1271 Witek, M. L., Garay, M. J., Diner, D. J., Bull, M. A., Seidel, F. C., Nastan, A. M., and  
1272 Hansen, E. G.: Introducing the MISR level 2 near real-time aerosol product, *Atmos.*  
1273 *Meas. Tech.*, 14, 5577–5591, <https://doi.org/10.5194/amt-14-5577-2021>, 2021.
- 1274 Wong, M. S., Shahzad, M. I., Nichol, J. E., Lee, K. H., and Chan, P. W.: Validation of  
1275 MODIS, MISR, OMI, and CALIPSO aerosol optical thickness using ground-based  
1276 sunphotometers in Hong Kong, *Int. J. Remote Sens.*, 34, 897–918,  
1277 <https://doi.org/10.1080/01431161.2012.720739>, 2013.
- 1278 Xu, H., Xue, Y., Guang, J., Li, Y., Yang, L., Hou, T., He, X., Dong, J., and Chen, Z.: A semi-  
1279 empirical optical data fusion technique for merging aerosol optical depth over China, in:  
1280 2012 IEEE International Geoscience and Remote Sensing Symposium, 2524–2527,  
1281 <https://doi.org/10.1109/IGARSS.2012.6350338>, 2012.
- 1282 Zhang, F. and O’Donnell, L. J.: Support vector regression, in: *Machine Learning*, Elsevier,  
1283 123–140, <https://doi.org/10.1016/B978-0-12-815739-8.00007-9>, 2020.
- 1284 Zhao, A., Li, Z., Zhang, Y., Zhang, Y., and Li, D.: Merging MODIS and ground-based fine  
1285 mode fraction of aerosols based on the geostatistical data fusion method, *Atmosphere*  
1286 (Basel)., 8, <https://doi.org/10.3390/atmos8070117>, 2017.
- 1287 Zhou, Y., Scavia, D., and Michalak, A. M.: Nutrient loading and meteorological conditions  
1288 explain interannual variability of hypoxia in Chesapeake Bay, *Limnol. Oceanogr.*, 59,  
1289 373–384, <https://doi.org/10.4319/lo.2014.59.2.0373>, 2014.
- 1290 Zimmerman, D., Pavlik, C., Ruggles, A., and Armstrong, M. P.: An experimental comparison  
1291 of ordinary and universal kriging and inverse distance weighting, *Math. Geol.*, 31, 375–  
1292 390, <https://doi.org/10.1023/A:1007586507433>, 1999.
- 1293